qNEP: A highly efficient neuroevolution potential with dynamic charges for large-scale atomistic simulations

Zheyong Fan,[1,2,*] Benrui Tang,[1,†] Esmée Berger,[3,†] Ethan Berger,[3] Erik Fransson,[3] Ke Xu,[1] Zihan Yan,[4] Zhoulin Liu,[5] Zichen Song,[6,7] Haikuan Dong,[1] Shunda Chen,[8] Lei Li,[6] Ziliang Wang,[9] Yizhou Zhu,[4] Julia Wiktor,[3] and Paul Erhart[3,10,‡]

[1] *College of Physical Science and Technology, Bohai University, Jinzhou, P. R. China*
[2] *Suzhou Laboratory, Suzhou, Jiangsu 215123, P. R. China*
[3] *Chalmers University of Technology, Department of Physics, 41296 Gothenburg, Sweden*
[4] *Department of Materials Science and Engineering, Westlake University, Hangzhou, Zhejiang 310030, China*
[5] *School of Science, Harbin Institute of Technology, Shenzhen 518055, Guangdong, P. R. China*
[6] *Shenzhen Key Laboratory of Micro/Nano-Porous Functional Materials (SKLPM), Department of Materials Science and Engineering, Southern University of Science and Technology, Shenzhen 518055, China*
[7] *Department of Materials Science and Engineering, City University of Hong Kong, Hong Kong SAR, China*
[8] *Department of Civil and Environmental Engineering, George Washington University, Washington, DC 20052, USA*
[9] *National Engineering Laboratory for Reducing Emissions from Coal Combustion, Shandong Key Laboratory of Green Thermal Power and Carbon Reduction, Shandong University, Jinan, Shandong, P. R. China*
[10] *Wallenberg Initiative Materials Science for Sustainability, Chalmers University of Technology, 41926 Gothenburg, Sweden*

(Dated: January 27, 2026)

Although electrostatics can be incorporated into machine-learned interatomic potentials, existing approaches are computationally very demanding, limiting large-scale, long-time simulations of electrostatics-driven phenomena such as dielectric response, infrared activity, and field–matter coupling. Here, we extend the neuroevolution potential (NEP), a highly efficient machine-learned interatomic potential, to a charge-aware framework (qNEP) by introducing explicit, environment-dependent partial charges. Each ionic partial charge is represented by a neural network as a function of the local descriptor vector, analogous to the NEP site-energy model. This formulation enables the direct prediction of the Born effective charge tensor for each ion and, consequently, the polarization. As a result, dielectric properties, infrared spectra, and coupling to external electric fields can be evaluated within a unified framework. We derive consistent expressions for the forces and virials that explicitly account for the position dependence of the partial charges. The qNEP method has been implemented in the free-and-open-source GPUMD package, with support for both Ewald summation and particle–particle particle–mesh treatments of electrostatics. We demonstrate the accuracy and efficiency of the qNEP approach through representative applications to water, $Li_7La_3Zr_2O_{12}$, $BaTiO_3$, and a magnesium–water interface. These results show that qNEP enables accurate atomistic simulations with explicit long-range electrostatics, scalable to million-atom systems on nanosecond time scales using consumer-grade GPUs.

I. INTRODUCTION

Machine-learned interatomic potentials (MLIPs) have become a widely adopted approach for accurate and efficient atomic-scale modeling of materials. Early MLIPs [1, 2] were inherently short-ranged. This approximation is adequate for many systems because of the shortsightedness of chemical bonding. However, short-ranged models become inadequate in systems with sizable partial charges and weak screening, where electrostatic interactions are intrinsically long-ranged. They are also limited when explicit coupling to external electric fields is required.

A common strategy to incorporate long-range electrostatics is to introduce fixed charges and subtract electrostatic contributions to energy and forces from the reference data [2–4]. A more flexible alternative employs a separate regression model, such as a neural network, to predict partial charges, as in third-generation high-dimensional neural network potentials [5, 6]. In this framework, partial charges are fitted to reference values obtained from a static charge decomposition scheme. Such an approach is conceptually unsatisfactory because there is no unique decomposition of the electronic charge density into individual ionic contributions. Other methods avoid explicit ionic charge partitioning by targeting higher-order electrostatic observables, such as the dipole moment [7], or by representing long-range electrostatics using the centers of maximally localized Wannier functions [8, 9].

More recently, charge equilibration schemes originally developed for conventional interatomic potentials [10, 11]

* brucenju@gmail.com; These authors contributed equally to this work.
† These authors contributed equally to this work.
‡ erhart@chalmers.se

have been adapted for use with MLIPs [12, 13]. In contrast to approaches in which partial charges are predicted directly by a regression model, charge equilibration schemes determine the charges self-consistently by minimizing an electrostatic energy functional subject to global constraints. This formulation enforces charge conservation and enables a physically consistent description of long-range charge transfer. Such schemes are employed, for example, in the fourth-generation high-dimensional neural network potential [12], but they substantially increase the computational cost due to the expensive charge equilibration step, even when iterative solvers are used for acceleration [14].

An alternative route to charge conservation is to start from the electric enthalpy and obtain the Born effective charges (BECs) as derivatives of the polarization. While this approach is physically elegant and internally consistent, current implementations [15] rely on equivariant neural networks, which are computationally demanding.

To circumvent the reliance on reference charges and to at least partly alleviate the need for explicit charge equilibration schemes, several approaches have been developed in which partial charges are not learned explicitly. Instead, they are treated as latent features of the model and determined implicitly by fitting the sum of the electrostatic energy and a short-range MLIP to the total target energies and forces. Song *et al.* [16] treated the partial charges by including both real-space (short-ranged) and reciprocal-space (long-ranged) electrostatic contributions, whereas Cheng *et al.* considered only the reciprocal-space (long-ranged) component [17, 18]. The latter, so-called latent Ewald summation (LES) approach, also enables the calculation of the polarization and BECs [19], and is available as a PyTorch-based library [20]. Related ideas have also been explored within a variational charge equilibration framework, which likewise enables the learning of partial charges without reference values [21].

Although the general principles for the incorporation of electrostatics into MLIPs have been established, existing approaches remain computationally demanding. As a result, their application to large-scale systems comprising hundreds of thousands to millions of atoms, as well as to long time scales extending from several to tens of nanoseconds, is severely constrained. This limits their use in studies of phenomena that critically depend on long-range electrostatics and polarization, such as ion and proton transport, charged defects and defect migration, dielectric response and vibrational or infrared spectroscopy, and field-driven polarization dynamics. Even for smaller systems, improving computational efficiency is essential to enable extensive sampling and an efficient use of modern computing resources.

In the present work, we therefore develop qNEP, a charge-aware MLIP that combines physical fidelity with high computational efficiency, enabling predictive simulations across broad classes of materials and extended length and time scales. The qNEP framework builds on the neuroevolution potential (NEP) scheme, a highly efficient short-ranged MLIP architecture with demonstrated accuracy and performance across a wide range of materials and applications [22–24]. Following earlier work [16, 17], we treat the partial charges as latent features of the model and obtain the BECs as derivatives of the polarization. Charge conservation is already strongly encouraged during training through an explicit regularization term. This requires only a small numerical adjustment during simulations to ensure physically consistent electrostatics. This formulation enables the direct computation of dielectric properties and infrared spectra, as well as a consistent coupling to external electric fields.

By implementing the particle-particle particle-mesh (PPPM) method [25] to evaluate electrostatic interactions during molecular dynamics (MD) simulations, we obtain a highly performant approach that is only 1.5 to 3 times slower than equivalently trained NEP models, while offering both enhanced functionality and improved accuracy. We demonstrate the accuracy and efficiency of qNEP through representative applications to water, $Li_7La_3Zr_2O_{12}$, $BaTiO_3$, and a magnesium–water interface. These results show that qNEP enables accurate atomistic simulations with explicit long-range electrostatics, scalable to million-atom systems on nanosecond time scales using consumer-grade GPUs.

II. METHODS

A. The original NEP model architecture

The qNEP approach introduced below is based on the NEP framework [26], which has undergone several refinements in recent years [27–29]. In this section, we provide a brief overview of the most recent version, NEP4 [29]. The term "neuroevolution" refers to the combination of a neural network (NN) model and an evolutionary training algorithm, namely the separable natural evolution strategy (SNES) [30].

The machine-learning model used in NEP is a feed-forward NN with a single hidden layer (Fig. 1a; blue output layer only). In terms of the NN model, the site energy can be explicitly expressed as

$$U_i = \sum_{\mu=1}^{N_{\rm neu}} w_\mu^{(1)} \tanh\left(\sum_{\nu=1}^{N_{\rm des}} w_{\mu\nu}^{(0)} D_\nu^i - b_\mu^{(0)}\right) - b^{(1)}, \quad (1)$$

where $\tanh(x)$ is the activation function, $w^{(0)}$ represents the weight parameters connecting the input layer (with dimension $N_{\rm des}$) and the hidden layer (with dimension $N_{\rm neu}$), $w^{(1)}$ represents the weight parameters connecting the hidden layer and the output layer (the site energy), $b^{(0)}$ represents the bias parameters in the hidden layer, and $b^{(1)}$ represents the bias parameter in the output layer. All of these parameters are trainable.

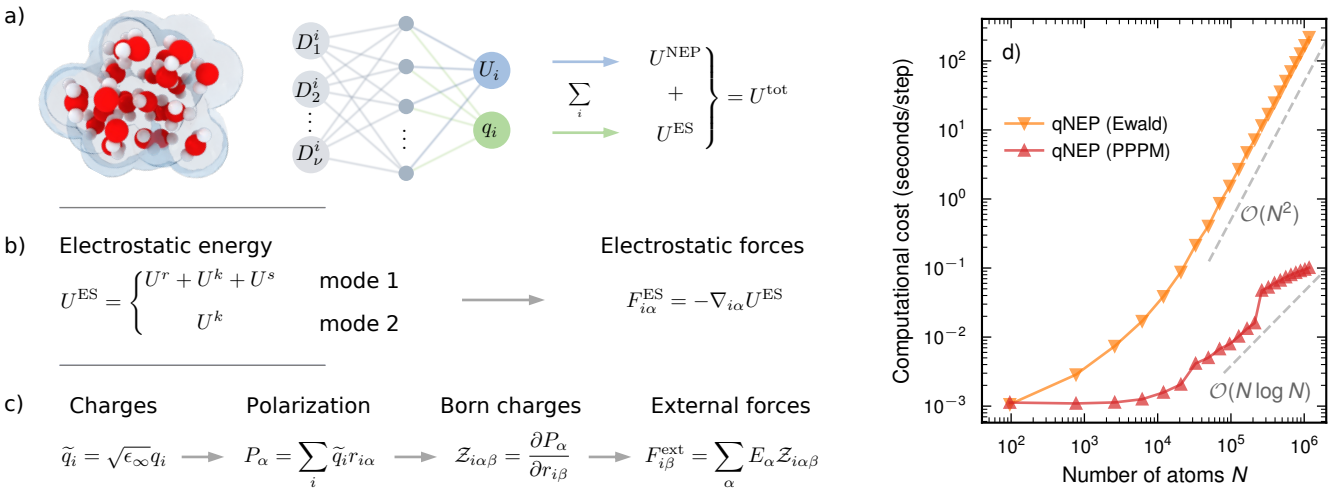

FIG. 1. Schematic illustration of the qNEP framework. (a) Neural network architecture of a qNEP model with two outputs: a site energy U_i and a partial charge q_i. The site energies are summed to yield the NEP contribution $U^{\rm NEP}$ (Sect. II A) to the total energy $U^{\rm tot}$, while interactions between the partial charges give rise to the electrostatic energy $U^{\rm ES}$ (Sect. II B). (b) Evaluation of the electrostatic energy and corresponding forces $\mathbf{F}_i^{\rm ES}$ (Sect. II C), including either both real- and reciprocal-space contributions (mode 1) or the reciprocal-space contribution only (mode 2). (c) Derived response properties obtained from the partial charges, such as the polarization $\mathbf{P}$, the Born effective charges $\mathcal{Z}_i$, and forces induced by external electric fields (Sect. II D). (d) Computational cost for evaluating the electrostatic contribution, comparing direct Ewald summation with the PPPM method (Sect. II F), which offers superior computational performance, particularly for large systems (shown here for water; Sect. III A).

The total energy is given by the sum of the site energies

$$U^{\rm NEP} = \sum_i U_i. \tag{2}$$

The input layer corresponds to the descriptor vector $\mathbf{D}^i$ (of dimension $N_{\rm des}$) for a given atom i, with its components denoted as D_ν^i in Eq. (1). Similar to the symmetry functions used in the Behler–Parrinello approach [1, 31], the descriptor components in NEP are classified into radial and angular ones. Both types of descriptors involve additional trainable parameters used to discriminate between atomic species. Details on the descriptor components and the associated trainable parameters can be found in Refs. 24, 28.

B. The qNEP model architecture

The qNEP approach extends the NEP framework by adding an additional output node to predict the partial charges q_i. Using separate NNs for the potential energy and the charges does not lead to a noticeable improvement in training accuracy, while increasing both the data requirements and the training cost. We therefore adopt a single-NN architecture (Fig. 1a; blue and green output layers).

Given the partial charges, the electrostatic energy $U^{\rm ES}$ is evaluated under periodic boundary conditions using the Ewald decomposition as the sum of three contributions,

$$U^{\rm ES} = U^{\rm r} + U^k + U^{\rm s}, \tag{3}$$

where $U^{\rm r}$ is the real-space component, U^k is the reciprocal-space component (evaluated in k-space, hence the superscript k), and $U^{\rm s}$ is the self-energy. The total energy in qNEP is given by the sum of the NEP energy and the electrostatic energy,

$$U^{\rm tot} = U^{\rm NEP} + U^{\rm ES}. \tag{4}$$

We consider two different modes for evaluating the energy contribution associated with the partial charges. In mode 1, both the real-space and reciprocal-space contributions are included (Fig. 1b), as adopted by Song *et al.* [16], and the electrostatic energy of the system is calculated according to Eq. (3). One may, however, argue that a short-ranged MLIP such as NEP already captures all short-range interactions, including the real-space component of electrostatics, making an explicit real-space electrostatic term potentially redundant. In mode 2, we therefore consider only the reciprocal-space contribution (Fig. 1b), as adopted by Cheng *et al.* [17, 18], i.e.,

$$U^{\rm ES} = U^k. \tag{5}$$

One of the aims of this work is to evaluate the relative advantages and disadvantages of these two approaches in realistic systems.

In the remainder of this section, we present explicit expressions for the real-space and reciprocal-space contributions to the electrostatic energy, as well as for the

self-energy. We then derive expressions for the force and virial (Sect. II C), as well as for the BEC tensor and related properties (Sect. II D). The latter enables coupling to external electric fields and the computation of quantities such as the dielectric function, infrared spectra, and ionic electrical conductivity.

During training of qNEP models, the NEP loss function is augmented with additional terms that penalize violations of charge conservation and, optionally, constrain the prediction of the BECs (Sect. II E). For the evaluation of reciprocal-space contributions, we implement both Ewald summation and the PPPM technique (Sect. II F). We have made functionality for training and deploying qNEP models available in the free-and-open-source GPUMD package [24] from version 4.6, together with the supporting CALORINE Python package from version 3.3 [32].

1. *Real-space electrostatic energy*

The real-space electrostatic energy included in U^{ES} when using mode 1 (Eq. (3)) is given by

$$U^{\mathrm{r}} = \frac{1}{2}\frac{1}{4\pi\epsilon_0}\sum_i\sum_{j\neq i}\frac{q_i q_j}{r_{ij}}\mathrm{erfc}(\alpha, r_{ij}), \tag{6}$$

where erfc denotes the complementary error function, r_{ij} is the distance between atoms i and j, q_i is the charge of atom i, and ϵ_0 is the vacuum permittivity. We use the terms "ion" and "atom" interchangeably, as it is conventional to use atom in the context of MLIPs, while partial charges are typically associated with ions. The real-space contribution is evaluated up to a cutoff radius r_{c}.

The parameter α, which has the dimension of inverse length, controls the relative convergence rates of the real-space and reciprocal-space components. Larger values of α lead to faster convergence in real space with respect to the cutoff radius r_{c}, whereas smaller values of α improve convergence in reciprocal space with respect to the cutoff wave vector k_{max} (see below). In this work, the real-space cutoff radius r_{c} is chosen to coincide with the pairwise cutoff of the associated NEP model, which typically lies in the range 4 Å to 8 Å. After fixing the NEP cutoff radius, we select α to provide sufficient accuracy for the real-space contribution. Specifically, we use $\alpha = \pi/r_{\mathrm{c}}$, which is a conventional choice to converge the real-space contribution [33].

2. *Reciprocal-space electrostatic energy*

The reciprocal-space contribution to the electrostatic energy, U^k, which is required in both mode 1 (Eq. (3)) and mode 2 (Eq. (5)), is given by

$$U^k = \frac{1}{4\pi\epsilon_0}\sum_{\mathbf{k}\neq\mathbf{0}}^{k<k_{\mathrm{max}}} G(k)S(\mathbf{k})S^*(\mathbf{k}), \tag{7}$$

where

$$S(\mathbf{k}) \equiv \sum_i q_i e^{-\mathrm{i}\mathbf{k}\cdot\mathbf{r}_i} = S^*(-\mathbf{k}) \tag{8}$$

is the structure factor. Here, $\mathbf{r}_i$ denotes the position of atom i, $\mathbf{k}$ is a reciprocal-space wave vector given by integer combinations of the reciprocal lattice basis vectors, and $k = |\mathbf{k}|$.

The function

$$G(k) \equiv \frac{2\pi}{\Omega}\frac{1}{k^2}e^{-k^2/4\alpha^2}, \tag{9}$$

where Ω is the volume of the simulation cell, corresponds to the product of the Green's function of the Coulomb potential and a Gaussian smoothing function. The summation over wave vectors $\mathbf{k}$ in Eq. (7) excludes the $\mathbf{k} = \mathbf{0}$ term, which corresponds to the total charge of the system, and is truncated at a maximum magnitude k_{max}. An accuracy of approximately 10^{-5}, consistent with that of the real-space contribution, is achieved by choosing $k_{\mathrm{max}} = 2\pi\alpha$.

3. *Self-energy*

For mode 1 (Eq. (3)), we also include the self-energy term, which removes the unphysical interaction of each charge with its own screening cloud,

$$U^{\mathrm{s}} = -\frac{1}{4\pi\epsilon_0}\frac{\alpha}{\sqrt{\pi}}\sum_i q_i^2, \tag{10}$$

which is consistent with the approach adopted by Song *et al.* [16].

C. Energy derivatives

Starting from the energy, one can derive other microscopic quantities such as the force and virial. A crucial aspect in the present context is that both static and dynamic contributions of the charges must be taken into account when evaluating energy derivatives. Here, static charge refers to contributions originating from the explicit $1/r$ dependence in the Coulomb energy, whereas dynamic charge refers to contributions arising from the position dependence of the charges themselves.

qNEP models are many-body potentials, and general expressions for the force and virial of such potentials have been discussed previously [34]. An important result is that Newton's third law (in its weak form) continues to hold for many-body potentials. Accordingly, the force acting on atom i can be expressed as a pairwise summation [34]

$$\mathbf{F}_i = \sum_{j\neq i}\left(\mathbf{F}_{ij} - \mathbf{F}_{ji}\right), \tag{11}$$

where $\mathbf{F}_{ij}$ can be interpreted as a "partial force" contribution.

Using the partial forces, the per-atom virial tensor can be written as [34]

$$\mathbf{W}_i = \sum_{j \neq i} \mathbf{r}_{ij} \otimes \mathbf{F}_{ji}. \tag{12}$$

Throughout this work, we define

$$\mathbf{r}_{ij} \equiv \mathbf{r}_j - \mathbf{r}_i \tag{13}$$

as the distance vector pointing from atom i to atom j.

Analogous to the electrostatic energy the force is evaluated using an Ewald decomposition into real-space, reciprocal-space, and self-energy contributions. For static charges, the real-space term gives rise to purely pairwise partial forces, while the reciprocal-space contribution is most naturally expressed as a per-atom force. When the charges depend on the atomic configuration, additional force contributions arise in all three parts of the Ewald sum through the chain rule, i.e., from terms proportional to $(\partial E/\partial q_i)(\partial q_i/\partial \mathbf{r})$. These dynamic-charge contributions can be cast into a partial-force form and combined consistently with the static terms, allowing the total force and virial to be evaluated within the same many-body framework.

We now present explicit expressions for the partial forces associated with the different energy contributions in the qNEP model. For the NEP contribution, the partial force can be written as

$$\mathbf{F}_{ij}^{\mathrm{NEP}} = \sum_{\nu=1}^{N_{\mathrm{des}}} \frac{\partial U_i}{\partial D_\nu^i} \frac{\partial D_\nu^i}{\partial \mathbf{r}_{ij}}. \tag{14}$$

Details on the derivatives of the descriptors with respect to atomic positions can be found in previous work [28]. For the electrostatic contribution, we discuss the three components separately in the following subsections.

For the contributions due to the dynamic charges the per-atom virial is obtained from the corresponding partial forces according to Eq. (12).

1. The real-space contribution

For static charges, the real-space contribution to the electrostatic energy is purely two-body (pairwise) in nature. Nevertheless, it can be formulated within the general many-body potential framework introduced above. Within this framework, the partial force can be derived as

$$\mathbf{F}_{ij}^{\mathrm{r,\ static}} = \frac{1}{2} \frac{-q_i q_j}{4\pi\epsilon_0} \frac{\mathbf{r}_{ij}}{r_{ij}^3} \left[\frac{2\alpha}{\sqrt{\pi}} r_{ij} e^{-\alpha^2 r_{ij}^2} + \mathrm{erfc}(\alpha\, r_{ij}) \right]. \tag{15}$$

When the charges are dynamic, i.e., explicitly dependent on the atomic configuration, an additional contribution to the partial force arises from the position dependence of the charges. This contribution is given by

$$\mathbf{F}_{ij}^{\mathrm{r,\ dynamic}} = \frac{1}{4\pi\epsilon_0} \frac{\partial q_i}{\partial \mathbf{r}_{ij}} \left(\sum_{k \neq i} \frac{q_k}{r_{ik}} \mathrm{erfc}(\alpha\, r_{ik}) \right). \tag{16}$$

The derivative of the charge with respect to the relative position vector is evaluated using the chain rule,

$$\frac{\partial q_i}{\partial \mathbf{r}_{ij}} = \sum_{\nu=1}^{N_{\mathrm{des}}} \frac{\partial q_i}{\partial D_\nu^i} \frac{\partial D_\nu^i}{\partial \mathbf{r}_{ij}}. \tag{17}$$

2. The reciprocal-space contribution

The force acting on atom i due to the reciprocal-space contribution of the electrostatic energy with static charges can be derived to be

$$\mathbf{F}_i^{k,\mathrm{static}} = 2 \frac{q_i}{4\pi\epsilon_0} \sum_{\mathbf{k} \neq \mathbf{0}}^{k<k_{\max}} \mathbf{k}\, G(k) \mathrm{Im}\left[S(\mathbf{k}) e^{i\mathbf{k}\cdot\mathbf{r}_i} \right]. \tag{18}$$

The partial force due to dynamic charges can be derived to be

$$\mathbf{F}_{ij}^{k,\mathrm{dynamic}} = 2 \sum_{\mathbf{k} \neq \mathbf{0}}^{k<k_{\max}} \frac{G(k)}{4\pi\epsilon_0} \mathrm{Re}\left[S(\mathbf{k}) \frac{\partial q_i}{\partial \mathbf{r}_{ij}} e^{i\mathbf{k}\cdot\mathbf{r}_i} \right]. \tag{19}$$

While the reciprocal-space contribution to the force due to static charges is usually not calculated in a pairwise manner, the virial can be calculated in a per-atom style [35],

$$\mathbf{W}_i^{k,\mathrm{static}} = \sum_{\mathbf{k} \neq \mathbf{0}}^{k<k_{\max}} \frac{G(k)\, q_i\, e^{i\mathbf{k}\cdot\mathbf{r}_i}\, S(\mathbf{k})}{4\pi\epsilon_0} \mathbf{B}. \tag{20}$$

Here, $\mathbf{B}$ is a k-space stress kernel that results from the derivative of the reciprocal-space electrostatic energy with respect to a homogeneous strain of the simulation cell and maps each $\mathbf{k}$-mode contribution onto a second-rank virial tensor,

$$\mathbf{B} = \mathbf{I} - \left(\frac{2}{4\alpha^2} + \frac{2}{k^2} \right) \mathbf{K}, \tag{21}$$

where $\mathbf{I}$ is the 3×3 identity tensor, and $\mathbf{K}$ is a tensor with components $K_{\alpha\beta} = k_\alpha k_\beta$. If the per-atom virial is not needed, the total virial can be more cheaply calculated as

$$\mathbf{W}^{k,\mathrm{static}} = \sum_{\mathbf{k} \neq \mathbf{0}}^{k<k_{\max}} \frac{G(k)|S(\mathbf{k})|^2}{4\pi\epsilon_0} \mathbf{B}. \tag{22}$$

Note that although $\mathbf{B}$ is a 3×3 tensor, it has only six independent components, reflecting the symmetry of the stress tensor and the fact that the reciprocal-space contribution ultimately derives from an underlying pairwise electrostatic interaction.

3. The self-energy contribution

For static charges, the self-energy does not contribute to the force, since it depends only on the fixed charge values and is therefore independent of the atomic positions. When the charges are configuration-dependent, however, the self-energy acquires an implicit position dependence through $q_i(\{\mathbf{r}\})$, which gives rise to an additional force contribution. In this case, the corresponding partial force is

$$\mathbf{F}_{ij}^{\mathrm{s,dynamic}} = -\frac{2}{4\pi\epsilon_0}\frac{\alpha}{\sqrt{\pi}} q_i \frac{\partial q_i}{\partial \mathbf{r}_{ij}}. \tag{23}$$

As in the other contributions, the derivative of the charge with respect to position is evaluated using the chain rule introduced above.

D. Born effective charge and related properties

The output charges q can be used to compute the macroscopic polarization $\mathbf{P}$ and the associated BECs (Fig. 1c), as first discussed by Zhong *et al.* [19] Before calculating the polarization, the learned partial charges need to be scaled [36]

$$\widetilde{q}_i = \sqrt{\epsilon_\infty} q_i, \tag{24}$$

where ϵ_∞ denotes the high-frequency relative permittivity, also known as the electronic dielectric constant. Using these notations, the Coulomb potential between two charges can be written as

$$\frac{1}{4\pi\epsilon_0}\frac{q_i q_j}{r_{ij}} = \frac{1}{4\pi\epsilon_0\epsilon_\infty}\frac{\widetilde{q}_i \widetilde{q}_j}{r_{ij}}. \tag{25}$$

This rescaling accounts for electronic screening effects that are not explicitly included in the ionic degrees of freedom. The learned partial charges q_i are thus screened charges, while the scaled charges $\widetilde{q}_i$ can be understood as naked charges. The high-frequency relative permittivity ϵ_∞ is material specific and is generally taken as a trainable parameter. In this work, we assume an isotropic dielectric constant, leaving an anisotropic extension for future work.

For non-periodic systems, where absolute positions are well defined, the polarization (which reduces to the dipole moment) can be written as

$$P_\alpha = \sum_i \widetilde{q}_i r_{i\alpha} \tag{26}$$

and the BEC tensors can be obtained as

$$\begin{aligned}\mathcal{Z}_{i\alpha\beta} = \frac{\partial P_\alpha}{\partial r_{i\beta}} &= \widetilde{q}_i\delta_{\alpha\beta} + \sum_j^N r_{j\alpha}\frac{\partial \widetilde{q}_j}{\partial r_{i\beta}} \\ &= \widetilde{q}_i\delta_{\alpha\beta} - \sum_{j\neq i}\left(r_{i\alpha}\frac{\partial \widetilde{q}_i}{\partial r_{ij\beta}} - r_{j\alpha}\frac{\partial \widetilde{q}_j}{\partial r_{ji\beta}}\right),\end{aligned} \tag{27}$$

where the second expression follows from rewriting the derivatives in terms of relative position vectors. For periodic systems, absolute positions are not well defined, and the polarization must be expressed in a translationally invariant form,

$$\mathcal{Z}_{i\alpha\beta} = \widetilde{q}_i\delta_{\alpha\beta} + \frac{1}{2}\sum_{j\neq i}\left(r_{ij\alpha}\frac{\partial \widetilde{q}_i}{\partial r_{ij\beta}} - r_{ji\alpha}\frac{\partial \widetilde{q}_j}{\partial r_{ji\beta}}\right). \tag{28}$$

Using the BEC, the force acting on ion i in response to an external electric field $\mathbf{E}$ can be written as

$$F_{i\beta}^{\mathrm{ext}} = \sum_\alpha E_\alpha \mathcal{Z}_{i\alpha\beta}. \tag{29}$$

During MD simulations, the time derivative of the polarization corresponds to the ionic electric current and can be evaluated from the BEC and the atomic velocities $\mathbf{v}$ as

$$\dot{P}_\alpha = \frac{\mathrm{d}P_\alpha}{\mathrm{d}t} = \sum_{i=1}^N\sum_\beta \mathcal{Z}_{i\alpha\beta} v_{i\beta}. \tag{30}$$

The polarization along the trajectory can then be obtained by time integration of $\dot{P}_\alpha$, provided that the initial value is known. The Fourier transform of the time autocorrelation function (ACF) $\langle \dot{\mathbf{P}}(0)\cdot\dot{\mathbf{P}}(t)\rangle$ is proportional to the infrared spectrum, while its time integral yields the ionic electrical conductivity

$$\sigma = \frac{1}{3k_{\mathrm{B}}TV}\int_0^\infty \langle \dot{\mathbf{P}}(0)\cdot\dot{\mathbf{P}}(t)\rangle \mathrm{d}t. \tag{31}$$

E. Training of the models

All parameters in the descriptor and the NN for the potential energy and partial charges are trainable, including the high-frequency relative permittivity ϵ_∞. As in the original NEP approach, these parameters are optimized using the SNES method [30]. The optimization is guided by a loss function, which we denote as $L(\mathbf{z})$, where the abstract vector $\mathbf{z}$ collects all trainable parameters.

The loss function is defined as a weighted sum of the root-mean-square error (RMSE) values for the energies (Δ_{e}), forces (Δ_{f}), virials (Δ_{v}), BECs ($\Delta_{\mathcal{Z}}$), and total charges (Δ_{Q}), together with $\mathcal{L}_1$ and $\mathcal{L}_2$ regularization terms,

$$\begin{aligned}L(\mathbf{z}) = \lambda_{\mathrm{e}}\Delta_{\mathrm{e}}(\mathbf{z}) + \lambda_{\mathrm{f}}\Delta_{\mathrm{f}}(\mathbf{z}) + \lambda_{\mathrm{v}}\Delta_{\mathrm{v}}(\mathbf{z}) + \lambda_{\mathcal{Z}}\Delta_{\mathcal{Z}}(\mathbf{z}) \\ + \lambda_{\mathrm{Q}}\Delta_{\mathrm{Q}}(\mathbf{z}) + \lambda_1\|\mathbf{z}\|_1 + \lambda_2\|\mathbf{z}\|_2^2.\end{aligned} \tag{32}$$

Here, Δ_{Q} refers to the total charge of each structure rather than to individual partial charges and is included to penalize violations of charge conservation. This penalty ensures that the predicted total charge deviates from the target value only marginally.

To enforce strict charge conservation or charge neutrality, a final total-charge correction is applied before

evaluating the electrostatic energy and the BECs. Specifically, the scaled charges $\widetilde{q}_i$ in a system with N atoms are corrected as follows,

$$\widetilde{q}_i \to \widetilde{q}_i - \frac{1}{N}\sum_i (Q - \widetilde{q}_i), \tag{33}$$

where Q is the target total charge of the structure, which is zero in all the cases studied in this work. With the penalization term $\lambda_{\mathrm{Q}}\Delta_{\mathrm{Q}}(\mathbf{z})$ in the loss function, the total charge of the structure is already close to the target Q and the correction above mainly serves to ensure strict charge conservation that can be important in, e.g., simulations with an external electric field.

The inclusion of target BECs in the loss function is optional, and reference data need only be provided for a subset of the training structures. This makes it possible to limit the number of reference BEC calculations, which are computationally more demanding than calculations of energies, forces, or virials.

F. Accelerated calculation of the reciprocal-space contribution using PPPM

In the preceding sections, we assumed a direct Ewald summation for evaluating the reciprocal-space contribution to the electrostatic energy. In practical simulations, however, the use of fast Fourier transform (FFT)-based methods can significantly reduce the computational cost [37]. This leads to particle–mesh approaches such as PPPM [25], particle–mesh Ewald (PME) [38], and smooth PME (SPME) [39], which are closely related and can be mathematically transformed into one another [40, 41]. Here, we adopt the PPPM method and extend it to consistently account for both static and dynamic partial charges.

Within the PPPM framework, the reciprocal-space contribution to the electrostatic energy retains the formal structure of Eq. (7), but the Green's function factor $G(k)$ is replaced by an optimized counterpart, $G^{\mathrm{opt}}(\mathbf{k})$ [37],

$$U^k = \frac{1}{4\pi\epsilon_0}\sum_{\mathbf{k}\neq\mathbf{0}} G^{\mathrm{opt}}(\mathbf{k}) S(\mathbf{k}) S^*(\mathbf{k}). \tag{34}$$

The structure factor $S(\mathbf{k})$ is evaluated on a regular mesh of dimension $N_x \times N_y \times N_z$. Mesh charges are obtained by interpolating the original partial charges using a charge assignment function $W(\mathbf{r}_i - \mathbf{r}_s)$ [37], which specifies the fraction of the charge at position $\mathbf{r}_i$ assigned to the mesh point $\mathbf{r}_s$. The charge assignment function can be decomposed into the three Cartesian directions,

$$W(\mathbf{r}_i - \mathbf{r}_s) = W(x_i - x_s)\, W(y_i - y_s)\, W(z_i - z_s). \tag{35}$$

Explicit expressions for the charge assignment functions for interpolation orders $P = 1$ to $P = 7$ are given by Deserno and Holm [40].

In our implementation, we use a mesh spacing smaller than 1 Å together with an interpolation order $P = 5$, which yields an accuracy of approximately 10^{-4}. The corresponding optimized Green's function is given by [37, 41]

$$G^{\mathrm{opt}}(\mathbf{k}) = \frac{G(k)\left[\prod_{\alpha=1}^{3} \mathrm{sinc}^P\left(\frac{\pi n_\alpha}{N_\alpha}\right)\right]^2}{\prod_\alpha^3 \left(1 - \frac{5}{3}z_\alpha^2 + \frac{7}{9}z_\alpha^4 + \frac{17}{189}z_\alpha^6 + \frac{2}{2835}z_\alpha^8\right)}, \tag{36}$$

where $\mathrm{sinc}(x) = \sin(x)/x$, $z_\alpha = \sin(\pi n_\alpha / N_\alpha)$, and n_α are integer mesh indices satisfying $-N_\alpha/2 \le n_\alpha < N_\alpha/2$.

The reciprocal-space force due to static charges can be computed in several equivalent ways [37]. Here, we employ the i$\mathbf{k}$-differentiation scheme,

$$\mathbf{F}_i^{k,\mathrm{static}} = -\frac{2}{4\pi\epsilon_0} q_i \sum_{\mathbf{r}_s} W(\mathbf{r}_i - \mathbf{r}_s)\mathcal{F}^{-1}\left[\mathrm{i}\mathbf{k} S(\mathbf{k}) G^{\mathrm{opt}}(\mathbf{k})\right]. \tag{37}$$

For dynamic charges, the force contribution arises from the explicit position dependence of the charges and is evaluated using an analytical differentiation scheme,

$$\mathbf{F}_{ij}^{k,\mathrm{dynamic}} = \frac{2}{4\pi\epsilon_0}\frac{\partial q_i}{\partial \mathbf{r}_{ij}} \sum_{\mathbf{r}_s} W(\mathbf{r}_i - \mathbf{r}_s)\, \mathcal{F}^{-1}\left[S(\mathbf{k}) G^{\mathrm{opt}}(\mathbf{k})\right]. \tag{38}$$

For the reciprocal-space contribution to the virial arising from static charges, the total virial can be evaluated analogously to Eq. (22). If a per-atom decomposition is required, the per-atom virial can be written as

$$\mathbf{W}_i^{k,\mathrm{static}} = \frac{q_i}{4\pi\epsilon_0} \sum_{\mathbf{r}_s} W(\mathbf{r}_i - \mathbf{r}_s)\, \mathcal{F}^{-1}\left[S(\mathbf{k}) G^{\mathrm{opt}}(\mathbf{k})\mathbf{B}\right]. \tag{39}$$

A forward FFT is used to compute $S(\mathbf{k})$ from the charge mesh, while backward FFTs are used to evaluate the forces and virials, as indicated by the $\mathcal{F}^{-1}$ operations. Specifically, three backward FFTs are required to obtain the three Cartesian components of the force due to static charges according to Eq. (37), and one backward FFT is required to obtain the force contribution due to dynamic charges according to Eq. (38). If the per-atom virial is needed, six backward FFTs are required to evaluate the six independent components of the virial tensor according to Eq. (39). Efficient implementations of these operations can be realized using standard libraries from the CUDA and HIP toolkits.

The resulting PPPM implementation exhibits an overall $\mathcal{O}(N \log N)$ scaling with the number of atoms due to the use of FFTs, in contrast to the quadratic scaling of the direct Ewald summation. In practice, the PPPM method features a small prefactor and near-linear scaling over the system sizes considered here, resulting in a computational cost that is one to several orders of magnitude lower than for the Ewald approach (Fig. 1d).

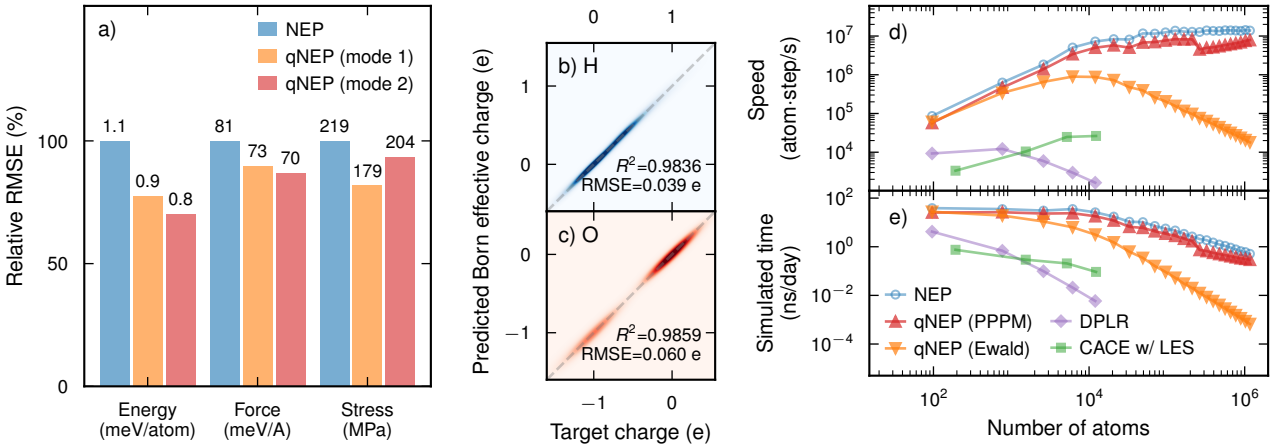

FIG. 2. **Performance of qNEP for water.** (a) Relative validation RMSEs of NEP and qNEP models. (b,c) Parity plots of Born effective charges for H and O, respectively, obtained from the qNEP model trained on the full reference data set using mode 2. (d,e) Performance comparison of qNEP models with NEP, a CACE model with LES, and a deep potential model with long-range electrostatic interactions (DPLR), in terms of (d) computational speed and (e) the simulated time achievable within one day on a single Nvidia RTX4090 GPU using a time step of 0.5 fs.

III. RESULTS

To illustrate the potential of the qNEP approach, we constructed models for several distinct classes of materials and employed them in prototypical applications. In the following section (Sect. III A), we consider water as a representative liquid system. We show that the inclusion of electrostatics in qNEP models systematically improves accuracy compared to regular NEP models at only a modest additional computational cost. The resulting models enable simulations of water systems comprising hundreds of thousands or even millions of atoms and allow for simulation times of several tens of nanoseconds per day on a single GPU. We further demonstrate the capability of qNEP models to predict the infrared spectrum of water as a function of temperature.

We then turn to two crystalline systems, again observing systematic improvements upon including electrostatics. First, for the prototypical ionic conductor $Li_7La_3Zr_2O_{12}$, we show that the temperature dependence of the structural parameters and the transition from the low-temperature tetragonal phase to the high-temperature cubic phase are in close agreement with experimental data (Sect. III B). Further analysis reveals a qualitative change in the charge distribution across the phase transition, which is reflected in the ionic electrical conductivity, with the activation energy decreasing from 1.45 eV in the tetragonal phase to 0.29 eV in the cubic phase.

Next, we consider the prototypical ferroelectric $BaTiO_3$, demonstrating that qNEP models readily reproduce not only the experimentally observed phase transitions and structural changes, but also the associated evolution of the polarization (Sect. III C). We map out polarization–electric field (poling) loops at different temperatures, illustrating the coupling to external electric fields. In addition, we extract the temperature dependence of both the dielectric function and the dielectric constant.

Finally, we examine magnesium corrosion in aqueous media, a reactive solid–liquid interface that combines metallic and insulating components (Sect. III D). The qNEP approach captures the diverse, environment-dependent charge states present in this system and, owing to its computational efficiency, enables simulations of the conversion of metallic Mg into hydroxylated and solvated species under highly reactive conditions over timescales of many nanoseconds.

A. Liquid water

Water is a representative liquid system, in which the electrostatic between the components plays an important role. To train models, we employed the data set of Zhang *et al.* [44] as curated by Xu *et al.* [42], who provided a split into 1388 training and 500 validation structures. All structures contain 384 atoms, and energies, forces, and stresses were obtained from density-functional theory (DFT) calculations using the strongly constrained and appropriately normed semilocal density functional (SCAN) exchange–correlation functional [45] (see Refs. 42, 44 for details). In addition, to enable learning of the dielectric response, we computed BECs for 195 structures randomly selected from the original data set (see Supp. Note 3 for details) [46–48]. We trained one NEP model and two qNEP models (one for each electrostatic mode) using identical hyperparameters (Supp. Note 2, Fig. S1).

The RMSEs demonstrate a systematic improvement

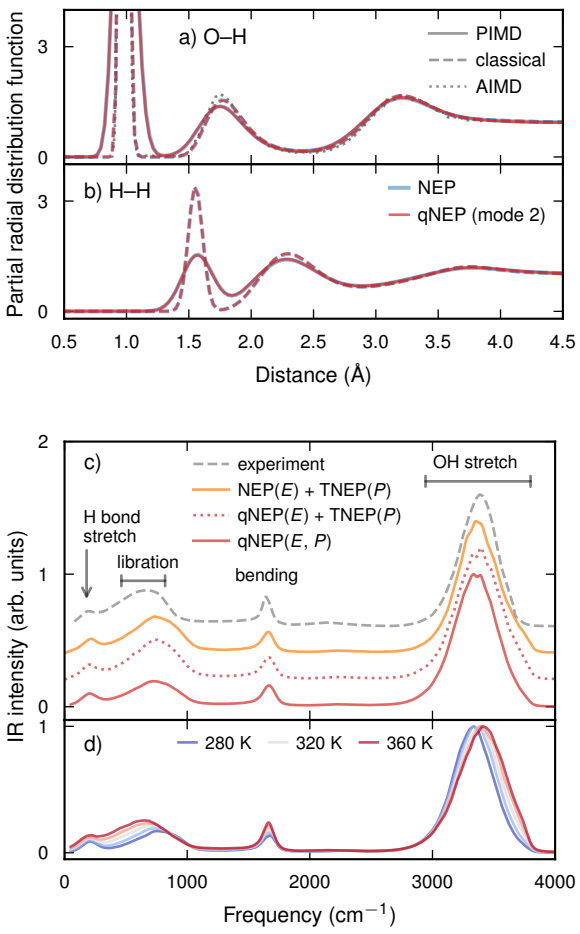

FIG. 3. **Properties of water with NEP and qNEP models.** (a,b) Partial radial distribution functions for (a) O–H and (b) H–H pairs in liquid water at 300 K. Solid and dashed lines correspond to quantum simulations performed using PIMD and classical simulations using standard MD, respectively, for the NEP (blue) and qNEP (red) models. Classical ab-initio MD (AIMD) reference data (dotted line) from Ref. 42 are included for comparison. (c,d) Infrared spectra obtained from classical MD simulations via the time ACF of the ionic electric current $\dot{\mathbf{P}}$. (c) Spectra obtained using different combinations of the NEP and qNEP (mode 2) models for sampling the energy landscape (E) and the TNEP (from Ref. 43) and qNEP models for computing the polarization (P) in comparison with experiment. (d) Temperature dependence of infrared spectra obtained using the qNEP model (mode 2) for both E and P.

in the accuracy of energies, forces, and stresses for the qNEP models compared to the NEP model (Fig. 2a), highlighting the importance of long-range electrostatic interactions in water. The two qNEP variants perform very similarly with the model trained using only the reciprocal-space contribution (mode 2) yielding marginally lower errors for energies and forces. This trend, which is also observed for the other systems discussed below, suggests that explicitly including short-ranged electrostatic interactions may be redundant when such interactions are already captured by the underlying short-ranged MLIP. Both qNEP models accurately reproduce the BECs (Fig. 2b,c; see Fig. S2 for the mode 1 model).

The qNEP models also learn the square root of the high-frequency dielectric constant, $\sqrt{\epsilon_\infty}$, which appears in Eq. (33) and corresponds to the refractive index at optical frequencies, n. Although $\sqrt{\epsilon_\infty}$ primarily acts as a hyperparameter during training, it is noteworthy that the fitted values, $\sqrt{\epsilon_\infty} = n = 1.77$ and 1.53 for modes 1 and 2, respectively, are in reasonable agreement with the experimental value of 1.33 at ambient conditions [49, 50]. Such a comparison is meaningful here because ϵ_∞ can be expected to be relatively homogeneous over the training domain.

Computational efficiency is critical for production simulations. The NEP model achieves speeds exceeding 10^7 atom step/s on a single consumer-grade GPU (Nvidia RTX 4090) for systems containing at least 10^4 atoms (Fig. S4). Using a time step of 0.5 fs, this corresponds to up to 40 ns of MD simulation per day (Fig. 2e; see also Fig. S4 for results on other GPUs). When employing qNEP models together with the PPPM method, the computational cost increases only by about a factor of two (Fig. 2e and Fig. S5). These numbers are several orders of magnitude higher than those achievable with, for example, a CACE model with LES [17] or a deep potential model with long-range electrostatic interactions [8].

As an additional validation, we computed partial radial distribution functions from both classical and PIMD simulations (Fig. 3a,b; Supp. Note 4) [51, 52]. The results are essentially indistinguishable between the NEP and qNEP models and are in very good agreement with ab initio MD simulations performed using the same exchange–correlation functional [42].

Finally, the availability of BECs combined with the high computational efficiency of qNEP models enables straightforward calculation of infrared spectra from the time ACF of the polarization or its time derivative [43] (see Supp. Note 4 for details). At room temperature, the resulting infrared spectra compare well with experimental reference data [53, 54], with remaining deviations attributable to the underlying exchange–correlation functional (Fig. 3c). Upon increasing temperature, we observe a blueshift of the O–H stretching band and a redshift of the librational band (Fig. 3d), both of which can be attributed to a weakening of intermolecular vibrational coupling.

B. Lithium lanthanum zirconate crystal

Garnet-type LLZO is among the most promising solid electrolyte materials for next-generation all-solid-state lithium batteries, combining high ionic conductivity with excellent chemical and electrochemical stability against

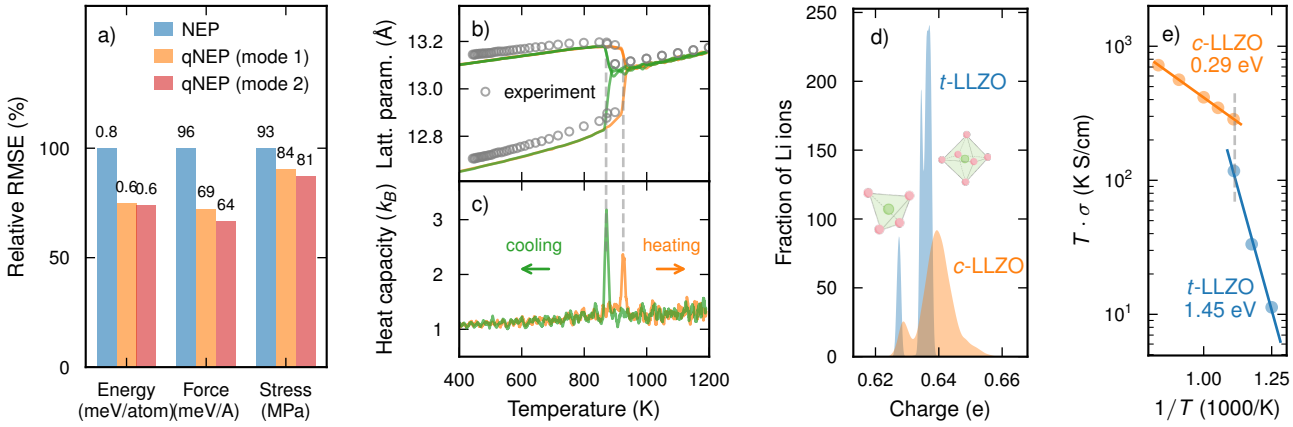

FIG. 4. **Garnet-type lithium lanthanum zirconate $Li_7La_3Zr_2O_{12}$ (LLZO).** (a) Relative training RMSEs of NEP and qNEP models, with RMSE values reported above the corresponding columns. (b,c) Temperature dependence of (b) lattice parameters and (c) heat capacity obtained from heating and cooling simulations. Vertical dashed lines indicate the corresponding phase transition temperatures. Experimental data for the lattice parameters from Ref. 55. (d) Distribution of Li partial charges in the tetragonal (t-LLZO) and cubic (c-LLZO) phases after structural relaxation. The left-hand peaks in the distributions correspond to Li-ions occupying tetrahedral sites (see inset) while the right-hand peaks correspond to octahedral sites (see inset). (e) Arrhenius plot of the ionic conductivity σ multiplied by temperature T. Activation energies extracted for the tetragonal and cubic phases are indicated. The vertical dashed line marks the average transition temperature of 900 K obtained from heating and cooling runs.

lithium metal [56]. Its garnet structure consists of a mobile Li-ion sublattice embedded within a rigid three-dimensional framework formed by interconnected LaO_8 dodecahedra and ZrO_6 octahedra, which creates fast diffusion pathways for Li-ions. As an ionic crystalline solid electrolyte, LLZO represents an ideal test case for assessing the importance of incorporating charge information into MLIPs, since electrostatic interactions between charged species play a central role in ionic transport. In addition, LLZO undergoes a well-known temperature-driven phase transition at approximately 900 K, from a low-temperature tetragonal phase (t-LLZO, $I4_1/acd$, ITC number 142) to a high-temperature cubic phase (c-LLZO, $Ia\bar{3}d$, ITC number 230). This transition is accompanied by an increase in the lithium ionic conductivity by several orders of magnitude [57] and has an order–disorder character, involving a reorganization of the Li-ion sublattice from an ordered arrangement with fully occupied sites in t-LLZO to a disordered state with partially occupied sites in c-LLZO. The combination of strong electrostatic interactions and complex structural phase behavior makes LLZO a demanding and representative benchmark for evaluating the qNEP approach.

We trained NEP and qNEP models (Supp. Note 5) using the data set of Yan and Zhu [57], which comprises 1978 configurations of pristine LLZO with energies, forces, and stresses computed using the PBEsol exchange–correlation functional [58]. Consistent with the trends observed for liquid water, the qNEP models reduce the RMSEs for energies, forces, and stresses by approximately 20 % to 30 % relative to the regular NEP model (Fig. 4a; see also Fig. S6).

Using the qNEP model trained in mode 2, we investigated the temperature dependence of the LLZO structure through heating and cooling simulations performed at a rate of 50 K/ns (Supp. Note 6) [59]. The resulting lattice parameters, and in particular the thermal expansion, are in good agreement with experimental measurements over the full temperature range considered [55] (Fig. 4b). Our simulations capture the phase transition from t-LLZO to c-LLZO at approximately 900 K, which is in excellent agreement with experimental observations. Additionally, a hysteresis of about 55 K is observed between the heating and cooling cycles (Fig. 4c).

The environment-dependent dynamic charges predicted by the qNEP model enable a detailed analysis of the order–disorder transition in LLZO. We relaxed snapshots extracted from MD trajectories of both t-LLZO and c-LLZO and evaluated the distributions of Li-ion charges in each phase (Fig. 4d). In t-LLZO, the charge distribution exhibits a lower-charge peak associated with Li-ions occupying tetrahedral sites (Wyckoff position 8a) and a higher-charge peak corresponding to ions in octahedral sites (16f and 32g). The octahedral contribution further displays a split structure, which we attribute to the distinct occupations of the 16f and 32g Wyckoff sites, both of which are octahedrally coordinated but feature slightly different local environments. In c-LLZO, the charge distribution becomes broader, reflecting the disordered nature of the Li-ion sublattice in the cubic phase.

These structural and charge-distribution differences between t-LLZO and c-LLZO are directly reflected in the transport properties (Fig. 4e). In particular, the ionic conductivity exhibits a pronounced reduction in activa-

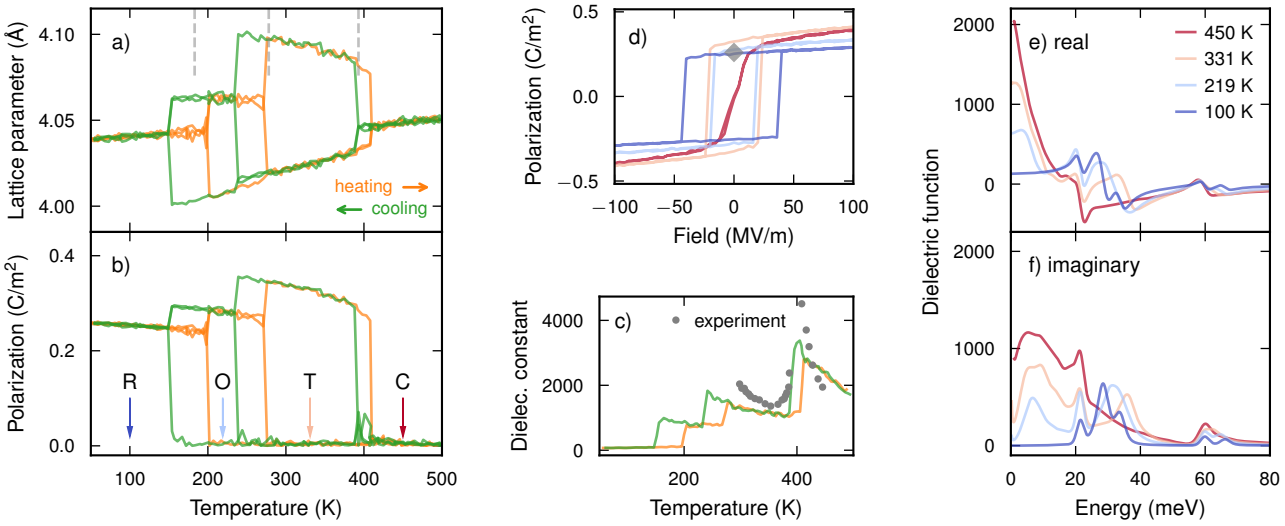

FIG. 5. **Ferroelectricity and dielectric response in barium titanate ($BaTiO_3$).** (a–c) Temperature dependence of (a) the lattice constant, (b) the polarization, and (c) the dielectric constant during heating and cooling, revealing the sequence of phase transitions from the rhombohedral (R) ground state through the orthorhombic (O) and tetragonal (T) phases to the high-temperature cubic (C) phase. Vertical dashed lines indicate the experimentally observed transition temperatures [60]. Experimental data points in (c) from Ref. 61. (d) Polarization–electric field (P–E) hysteresis loops and (e,f) the real and imaginary parts of the dielectric function at different temperatures, corresponding to all four phases (indicated by arrows in (b)). The gray diamond in (d) marks the experimental value for the spontaneous polarization at room temperature [62].

tion energy, decreasing from 1.45 eV in t-LLZO to 0.29 eV in c-LLZO. The latter value is in good agreement with experimental data in the high-temperature region [63]. The activation energy in t-LLZO is known to be highly sensitive to composition [57], whence a direct comparison is not possible but a possible target for future work.

C. Barium titanate

Next, we consider the prototypical ferroelectric perovskite $BaTiO_3$, which provides an ideal test case for evaluating qNEP models in the presence of strong electromechanical coupling and external electric fields. At low temperatures, $BaTiO_3$ adopts a rhombohedral structure with an instantaneous polarization along the ⟨111⟩ direction due to off-centering of the Ti atoms [60, 66]. Upon heating, it undergoes a sequence of phase transitions to orthorhombic and tetragonal phases at 183 K and 278 K, respectively, with polarization along the ⟨011⟩ and ⟨001⟩ directions [60]. At temperatures above 393 K, the material becomes paraelectric and cubic.

NEP and qNEP models were trained using a data set extended from Lindgren *et al.* [67] to 1832 structures, 1193 of which also included BECs (Supp. Note 7). Energies, forces, and stresses were obtained from DFT calculations [46] using the r2SCAN exchange–correlation functional [68], while BECs were obtained using the PBEsol functional [58] (Supp. Note 8). As in previous cases, the qNEP models achieve a higher accuracy than the corresponding NEP model. The qNEP model based on mode 1 and used for the simulations below achieves RMSEs of 1.2 meV/atom, 65 meV/Å, and 112 GPa for energies, forces, and stresses (Fig. S9). For comparison, the corresponding RMSEs for the NEP model are 1.0 meV/atom, 70 meV/Å, and 136 GPa. Both qNEP models also perform very well at predicting the BECs (Fig. S10).

The trained model correctly reproduces the sequence of four phases and yields transition temperatures of 151 K, 235 K, and 390 K, in good agreement with experiment (Fig. 5a; Supp. Note 9). This agreement can be attributed to the accuracy of the underlying exchange–correlation functional, whose energetics are faithfully reproduced by the qNEP model. A hysteresis of up to 50 K is observed between heating and cooling runs, even at the comparatively low rate of 10 K/ns used here. This behavior reflects the first-order nature of the phase transitions, despite their relatively small latent heats.

Using the predicted BECs, we directly computed the polarization as a function of temperature (Fig. 5b). All four phases are clearly resolved, with a pronounced polarization at low temperatures and a vanishing polarization above 407 K during heating and 390 K during cooling. The polarization increases when progressing from the rhombohedral through the orthorhombic to the tetragonal phase, in agreement with both shell-model simulations [69] and experimental measurements [60].

For selected temperatures representative of each phase, we further applied external electric fields to map

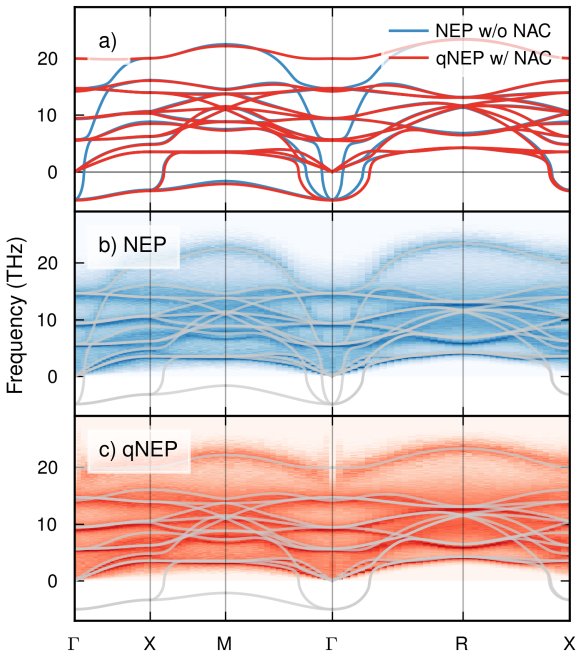

FIG. 6. **Phonons and LO–TO splitting in $BaTiO_3$.** (a) Harmonic phonon dispersion of the cubic phase obtained from NEP without non-analytic correction (NAC) and from qNEP including NAC, illustrating the longitudinal–transverse optical (LO–TO) splitting. Imaginary phonon frequencies are shown as negative values and indicate dynamically unstable modes. (b,c) Spectral energy density obtained from (b) NEP and (c) qNEP at 500 K in the cubic-phase region calculated with DYNASOR [64, 65]. Gray lines reproduce the corresponding harmonic phonon dispersions shown in (a).

out polarization–electric field (P–E) hysteresis loops (Fig. 5d; Supp. Note 9). As expected, the polarization can be switched by the applied field, and the spontaneous polarization in the absence of a field agrees well with the experimental value at room temperature [62] (indicated by the gray diamond in Fig. 5d). The coercive field depends sensitively on the switching frequency. Here, a frequency of 500 MHz was employed, which is low for MD simulations but still significantly higher than experimentally accessible frequencies [70]. A direct quantitative comparison of coercive fields is therefore not meaningful. Nevertheless, the computational efficiency of the qNEP approach opens the door to detailed investigations of switching mechanisms and domain-wall motion, particularly within multiscale simulation frameworks [71].

As a further validation, we computed the ionic contribution to the dielectric function from the time ACF of the ionic electric current (Supp. Note 9). The results reveal a strong dependence of the dielectric response on both temperature and frequency (Fig. 5e,f). Resonances appearing in the range 20 meV to 40 meV can be attributed to longitudinal optical modes at the Γ point. Their pronounced temperature dependence reflects the strong anharmonicity of $BaTiO_3$, which also gives rise to the very large dielectric constant observed (Fig. 5c; see also the static limit of the real part in Fig. 5e). The maximum dielectric constant obtained here reaches values of approximately 3000 on the high-temperature side of the tetragonal–cubic phase boundary, and is in good agreement with experimental measurements both in terms of magnitude and temperature dependence [61]. In this context, it is important to emphasize that the present simulations only include the ionic (vibrational) contribution while the experimental measurements also contain contributions from processes such as space-charge effects and grain boundaries. These occur on much longer time scales and their relative importance depends on sample preparation.

Finally, we examine the effect of long-range electrostatics on the phonon dispersion in the cubic phase. The harmonic phonon dispersions, calculated with PHONOPY [72, 73], predicted by the NEP and qNEP models agree closely over most of the Brillouin zone, except in the vicinity of the Γ point (Fig. 6a; Supp. Note 10). This difference arises from long-range Coulomb interactions, which lead to a splitting between longitudinal and transverse optical phonon branches. Accounting for this LO–TO splitting requires the application of non-analytic corrections (NACs), which in turn depend on knowledge of the BECs and are therefore only accessible within the qNEP framework. This distinction becomes even more pronounced in finite-temperature phonon dispersions obtained from the spectral energy density [74] using dynasor [64, 65] (Fig. 6b,c), where the LO and TO modes coincide at Γ for the NEP model but remain clearly separated for qNEP.

D. Corrosion of magnesium in water

Magnesium corrosion in aqueous media provides a prototypical example of a chemically reactive system in which accurate treatment of charge transfer is essential. Changes in the Mg valence state directly govern reaction pathways, intermediate species, and final corrosion products. In particular, the widely discussed incomplete-film monovalent magnesium-ion mechanism invokes the presence of a transient Mg^+ intermediate and remains controversial [75]. Resolving this issue is central to understanding the anomalous hydrogen evolution observed during magnesium corrosion and to guiding the design of corrosion-resistant magnesium alloys.

In previous studies, standard MLIPs were unable to explicitly represent evolving charge states and their associated long-range electrostatic interactions. This limitation hindered detailed investigations of charge evolution during the formation of corrosion intermediates and the dissolution dynamics of magnesium. The magnesium–water solid–liquid interface therefore constitutes a stringent and representative test case for qNEP models, as it directly probes their ability to capture environment-

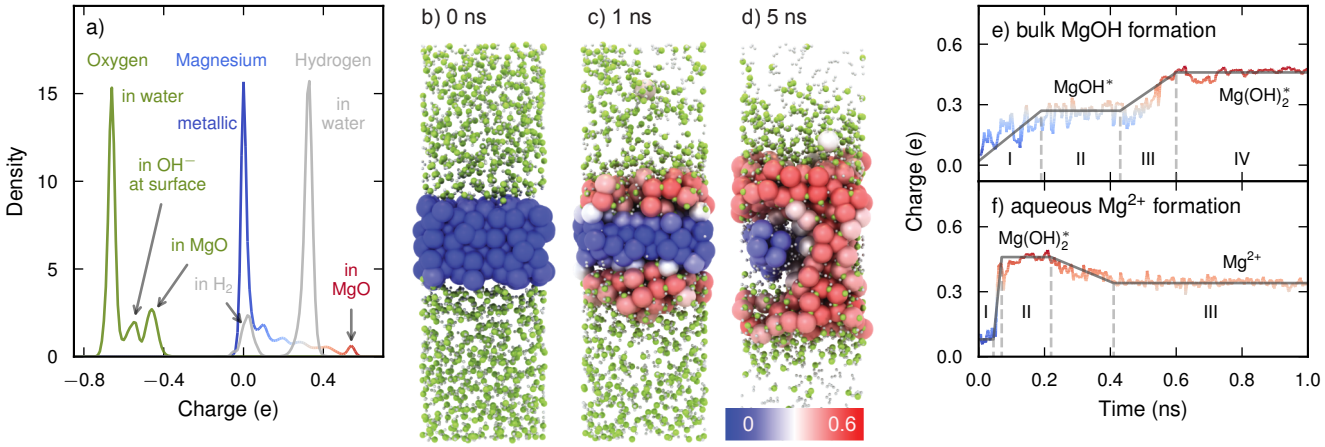

FIG. 7. **Corrosion of magnesium at a Mg–water interface.** (a) Distribution of atomic charges in the reference data set, distinguishing Mg, O, and H species across different chemical environments. (b–d) Representative snapshots from an MD simulation illustrating the conversion of metallic Mg (large blue spheres) into oxidized Mg species (large red spheres). The color scale (shown in (d)) indicates the Mg charge state. Oxygen and hydrogen atoms are shown as small green and gray spheres, respectively. (e,f) Two characteristic charge-evolution pathways of Mg: (e) formation of bulk magnesium hydroxide and (f) dissolution into aqueous Mg^{2+} ions. Asterisks (∗) denote adsorbed species.

dependent charge transfer in reactive chemical processes.

To train NEP and qNEP models, we employed the reference data set of Liu *et al.* [76], which systematically covers magnesium dissolution mechanisms (see Supp. Note 11 for details). The qNEP model achieves RMSEs values of 12 meV/atom for energies, 198 meV/Å for forces, and 824 GPa for stresses, representing a clear improvement over the NEP model, which yields 14 meV/atom, 230 meV/Å, and 787 GPa, respectively (Fig. S11). Crucially, the qNEP model successfully learns the relationship between local atomic environments and charge distributions (Fig. 7a). The predicted charges clearly distinguish different chemical states: Mg atoms in the metallic bulk exhibit charges close to zero, while Mg atoms in hydroxides or oxides carry positive charges. Oxygen atoms associated with water molecules, surface hydroxyl groups, and oxides likewise show distinct charge signatures.

MD simulations using the qNEP model therefore cannot only capture the structural evolution of the Mg–water interface, but also provide direct insight into transitions between different charge states. As a representative example, we consider the evolution of a highly reactive stepped Mg surface [77] in contact with water at 700 K over a simulation time of 5 ns that was recently analyzed using a NEP model (Fig. 7b–d). The detailed trajectories for such reactive systems are determined by a series of rare events, leading to considerable variety between individual simulations. Here, rather than repeating the comprehensive analysis from Ref. 76, we therefore applied our qNEP model to analyze a specific trajectory from this earlier work (see Supp. Note 12 for details).

After 1 ns (Fig. 7c), the system clearly separates into an upper hydroxide layer (red), a lower metallic Mg substrate (blue), and a transitional interfacial region containing partially hydroxylated Mg species (light gray/pink). In addition, a small number of Mg atoms undergo oxidation via dissolution into the aqueous phase. As corrosion proceeds, most of the metallic Mg is converted into hydroxylated species within 5 ns (Fig. 7d). While Mg atoms within the bulk metal and the corrosion product layer retain relatively stable valence states, atoms in the interfacial region exhibit distinct intermediate charge states corresponding to partial hydroxylation.

A detailed analysis of the charge trajectories reveals two characteristic corrosion pathways. The first pathway corresponds to the formation of solid-state corrosion products (Fig. 7e). Here, Mg atoms at the interface gradually increase their charge (stage I), followed by stabilization at an intermediate value associated with MgOH* species (stage II; the asterisk (∗) denotes an adsorbed species). During this stage, near-surface Mg atoms are hydroxylated, whereas atoms deeper in the substrate remain metallic. As OH* species migrate further inward (stage III), Mg undergoes deeper hydroxylation, forming amorphous $Mg(OH)_2$*, which can subsequently reorganize into crystalline $Mg(OH)_2$. Under conditions favoring the formation of a protective surface film, this pathway dominates.

The second pathway corresponds to the dissolution of hydrated Mg^{2+} ions into the aqueous phase (Fig. 7f). While the initial hydroxylation stages are similar to those of the solid-state pathway, Mg atoms located closer to the surface rapidly reach a divalent charge state (stage II, labeled $Mg(OH)_2$* in Fig. 7f). These Mg species then detach from the surface, leaving hydroxyl groups behind on the substrate, and form solvated Mg^{2+} ions in solution.

The qNEP model explicitly captures the competing mechanisms of solid-state oxidation and ionic dissolution, highlighting its ability to describe complex electrochem-

ical interfaces with evolving charge states. Overall, the application of qNEP to the Mg–water system not only reproduces key corrosion mechanisms identified in previous studies, but also provides dynamic, atom-resolved charge information that reveals the coupled evolution of valence states and structure during magnesium corrosion. This example demonstrates that qNEP overcomes key limitations of traditional MLIPs and enables efficient, large-scale simulations of charge-transfer-driven processes such as corrosion and electrocatalysis.

IV. SUMMARY AND CONCLUSIONS

We have introduced qNEP, a charge-aware extension of the highly efficient NEP framework that incorporates explicit long-range electrostatics while retaining the computational performance required for large-scale MD simulations. In qNEP, partial charges are learned as latent model features without relying on reference charge partitioning, charge conservation is enforced through a dedicated regularization term and a final total-charge correction, and polarization and BECs follow consistently as derivatives of the learned charges. By combining this formulation with an efficient PPPM implementation for reciprocal-space electrostatics, qNEP attains a computational cost only about 1.5 to 3 times higher than comparably trained NEP models, enabling simulations that extend to million-atom systems and nanosecond-to-tens-of-nanoseconds time scales on consumer-grade GPUs per day. Models that include the short-ranged electrostatic contribution explicitly (mode 1) and those that include only the long-ranged contribution (mode 2) yield similar accuracy.

Across representative liquid, ionic, ferroelectric, and reactive-interface systems, qNEP systematically improves the accuracy of energies, forces, and stresses relative to NEP while providing direct access to charge- and field-related observables. For water, qNEP delivers improved errors at modest overhead and enables infrared spectroscopy via the time ACF of the ionic electric current. For garnet-type $Li_7La_3Zr_2O_{12}$, qNEP captures the tetragonal–cubic transition and reveals phase-dependent charge distributions that correlate with the change in ionic transport barriers. For $BaTiO_3$, qNEP reproduces the sequence of ferroelectric phase transitions and enables predictions of polarization dynamics, dielectric response, and LO–TO splitting through NACs based on the predicted BECs. For magnesium corrosion in aqueous media, qNEP resolves environment-dependent charge states at a reactive solid–liquid interface and captures competing pathways of solid-state hydroxide formation and dissolution into aqueous Mg^{2+}. Together, these results establish qNEP as a practical and scalable route to accurate atomistic simulations of charge-transfer- and polarization-driven phenomena, opening the door to predictive studies of, e.g., transport, dielectric response, spectroscopy, and electrochemical reactivity across extended length and time scales.

Finally, we emphasize that the present work focuses exclusively on electrostatic interactions as the long-range contribution. Extensions of the qNEP framework to incorporate other long-range interactions, such as dispersion forces [78–80], constitute a natural and promising direction for future research. Such developments would further broaden the applicability of the NEP framework, in particular for aqueous, molecular, and biomolecular systems, where weak electronic screening in water renders electrostatic and other long-range interactions essential.

SUPPORTING INFORMATION

Additional technical information and figures (PDF).

DATA AVAILABILITY

The NEP and qNEP models as well as the reference data used for their training and validation have been deposited on Zenodo under accession code 10.5281/zenodo.18335947.

ACKNOWLEDGMENTS

ZF, BT, KX, and HD were supported by the Advanced Material National Science and Technology Major Project (grant No. 2025ZD0618902). EB, EB, EF, JW, and PE acknowledge funding from the Swedish Research Council (Nos. 2020-04935 and 2025-03999), the Knut and Alice Wallenberg Foundation (Nos. 2023.0032 and 2024.0042), the European Research Council (ERC Starting Grant No. 101162195), the Swedish Energy Agency (grant No. 45410-1), and the Swedish Strategic Research Foundation through a Future Research Leader programme (FFL21-0129). ZY and YZ acknowledge support from the National Natural Science Foundation of China (Nos. 22509162 and 225B2917). ZL and ZW acknowledge support from the Taishan Scholars Youth Expert Program of Shandong Province (tsqn202312002). ZS and LL acknowledge the Center for Computational Science and Engineering of the Southern University of Science and Technology. The computations were enabled by resources provided by the National Academic Infrastructure for Supercomputing in Sweden (NAISS) at C3SE, PDC, and NSC, partially funded by the Swedish Research Council through grant agreement no. 2022-06725, the Berzelius resource provided by the Knut and Alice Wallenberg Foundation at NSC, as well as the Open Source Super-computing Center of S-A-I.

[1] J. Behler and M. Parrinello, Generalized neural-network representation of high-dimensional potential-energy surfaces, Physical Review Letters **98**, 146401 (2007).

[2] A. P. Bartók, M. C. Payne, R. Kondor, and G. Csányi, Gaussian approximation potentials: The accuracy of quantum mechanics, without the electrons, Physical Review Letters **104**, 136403 (2010).

[3] K. Albe, J. Nord, and K. Nordlund, Dynamic charge-transfer bond-order potential for gallium nitride, Philosophical Magazine **89**, 3477 (2009).

[4] Z. Deng, C. Chen, X.-G. Li, and S. P. Ong, An electrostatic spectral neighbor analysis potential for lithium nitride, npj Computational Materials **5**, 75 (2019).

[5] N. Artrith, T. Morawietz, and J. Behler, High-dimensional neural-network potentials for multicomponent systems: Applications to zinc oxide, Physical Review B **83**, 153101 (2011).

[6] T. Morawietz, V. Sharma, and J. Behler, A neural network potential-energy surface for the water dimer based on environment-dependent atomic energies and charges, The Journal of Chemical Physics **136**, 064103 (2012).

[7] O. T. Unke and M. Meuwly, Physnet: A neural network for predicting energies, forces, dipole moments, and partial charges, Journal of Chemical Theory and Computation **15**, 3678 (2019).

[8] L. Zhang, H. Wang, M. C. Muniz, A. Z. Panagiotopoulos, R. Car, and W. E, A deep potential model with long-range electrostatic interactions, The Journal of Chemical Physics **156**, 124107 (2022).

[9] A. Gao and R. C. Remsing, Self-consistent determination of long-range electrostatics in neural network potentials, Nature Communications **13**, 1572 (2022).

[10] A. K. Rappe and W. A. I. Goddard, Charge equilibration for molecular dynamics simulations, The Journal of Physical Chemistry **95**, 3358 (1991).

[11] S. A. Ghasemi, A. Hofstetter, S. Saha, and S. Goedecker, Interatomic potentials for ionic systems with density functional accuracy based on charge densities obtained by a neural network, Physical Review B **92**, 045131 (2015).

[12] T. W. Ko, J. A. Finkler, S. Goedecker, and J. Behler, A fourth-generation high-dimensional neural network potential with accurate electrostatics including non-local charge transfer, Nature Communications **12**, 398 (2021).

[13] T. W. Ko, J. A. Finkler, S. Goedecker, and J. Behler, Accurate fourth-generation machine learning potentials by electrostatic embedding, Journal of Chemical Theory and Computation **19**, 3567 (2023).

[14] M. Gubler, J. A. Finkler, M. R. Schäfer, J. Behler, and S. Goedecker, Accelerating fourth-generation machine learning potentials using quasi-linear scaling particle mesh charge equilibration, Journal of Chemical Theory and Computation **20**, 7264 (2024).

[15] S. Falletta, A. Cepellotti, A. Johansson, C. W. Tan, M. L. Descoteaux, A. Musaelian, C. J. Owen, and B. Kozinsky, Unified differentiable learning of electric response, Nature Communications **16**, 4031 (2025).

[16] Z. Song, J. Han, G. Henkelman, and L. Li, Charge-optimized electrostatic interaction atom-centered neural network algorithm, Journal of Chemical Theory and Computation **20**, 2088 (2024).

[17] B. Cheng, Latent ewald summation for machine learning of long-range interactions, npj Computational Materials **11**, 80 (2025).

[18] D. S. King, D. Kim, P. Zhong, and B. Cheng, Machine learning of charges and long-range interactions from energies and forces, Nature Communications **16**, 8763 (2025).

[19] P. Zhong, D. Kim, D. S. King, and B. Cheng, Machine learning interatomic potential can infer electrical response (2025), arXiv:2504.05169 [cond-mat.mtrl-sci].

[20] D. Kim, X. Wang, S. Vargas, P. Zhong, D. S. King, T. J. Inizan, and B. Cheng, A universal augmentation framework for long-range electrostatics in machine learning interatomic potentials, Journal of Chemical Theory and Computation **21**, 12709 (2025).

[21] Y. Shaidu, F. Pellegrini, E. Küçükbenli, R. Lot, and S. de Gironcoli, Incorporating long-range electrostatics in neural network potentials via variational charge equilibration from shortsighted ingredients, npj Computational Materials **10**, 47 (2024).

[22] H. Dong, Y. Shi, P. Ying, K. Xu, T. Liang, Y. Wang, Z. Zeng, X. Wu, W. Zhou, S. Xiong, S. Chen, and Z. Fan, Molecular dynamics simulations of heat transport using machine-learned potentials: A mini-review and tutorial on GPUMD with neuroevolution potentials, Journal of Applied Physics **135**, 161101 (2024).

[23] P. Ying, C. Qian, R. Zhao, Y. Wang, K. Xu, F. Ding, S. Chen, and Z. Fan, Advances in modeling complex materials: The rise of neuroevolution potentials, Chemical Physics Reviews **6**, 011310 (2025).

[24] K. Xu, H. Bu, S. Pan, E. Lindgren, Y. Wu, Y. Wang, J. Liu, K. Song, B. Xu, Y. Li, T. Hainer, L. Svensson, J. Wiktor, R. Zhao, H. Huang, C. Qian, S. Zhang, Z. Zeng, B. Zhang, B. Tang, Y. Xiao, Z. Yan, J. Shi, Z. Liang, J. Wang, T. Liang, S. Cao, Y. Wang, P. Ying, N. Xu, C. Chen, Y. Zhang, Z. Chen, X. Wu, W. Jiang, E. Berger, Y. Li, S. Chen, A. J. Gabourie, H. Dong, S. Xiong, N. Wei, Y. Chen, J. Xu, F. Ding, Z. Sun, T. Ala-Nissila, A. Harju, J. Zheng, P. Guan, P. Erhart, J. Sun, W. Ouyang, Y. Su, and Z. Fan, GPUMD 4.0: A high-performance molecular dynamics package for versatile materials simulations with machine-learned potentials, Materials Genome Engineering Advances **3**, e70028 (2025).

[25] R. Hockney and J. Eastwood, *Computer simulation using particles* (Taylor & Francis, Inc., 1988).

[26] Z. Fan, Z. Zeng, C. Zhang, Y. Wang, K. Song, H. Dong, Y. Chen, and T. Ala-Nissila, Neuroevolution machine learning potentials: Combining high accuracy and low cost in atomistic simulations and application to heat transport, Physical Review B **104**, 104309 (2021).

[27] Z. Fan, Improving the accuracy of the neuroevolution machine learning potential for multi-component systems, Journal of Physics: Condensed Matter **34**, 125902 (2022).

[28] Z. Fan, Y. Wang, P. Ying, K. Song, J. Wang, Y. Wang, Z. Zeng, K. Xu, E. Lindgren, J. M. Rahm, A. J. Gabourie, J. Liu, H. Dong, J. Wu, Y. Chen, Z. Zhong, J. Sun, P. Erhart, Y. Su, and T. Ala-Nissila, GPUMD: A package for constructing accurate machine-learned potentials and performing highly efficient atomistic simulations, The Journal of Chemical Physics **157**, 114801 (2022).

[29] K. Song, R. Zhao, J. Liu, Y. Wang, E. Lindgren, Y. Wang, S. Chen, K. Xu, T. Liang, P. Ying, N. Xu, Z. Zhao, J. Shi, J. Wang, S. Lyu, Z. Zeng, S. Liang, H. Dong, L. Sun, Y. Chen, Z. Zhang, W. Guo, P. Qian, J. Sun, P. Erhart, T. Ala-Nissila, Y. Su, and Z. Fan, General-purpose machine-learned potential for 16 elemental metals and their alloys, Nature Communications **15**, 10208 (2024).

[30] T. Schaul, T. Glasmachers, and J. Schmidhuber, High dimensions and heavy tails for natural evolution strategies, in *Proceedings of the 13th Annual Conference on Genetic and Evolutionary Computation*, GECCO '11 (Association for Computing Machinery, New York, NY, USA, 2011) p. 845–852.

[31] J. Behler, Atom-centered symmetry functions for constructing high-dimensional neural network potentials, The Journal of Chemical Physics **134**, 074106 (2011).

[32] E. Lindgren, M. Rahm, E. Fransson, F. Eriksson, N. Österbacka, Z. Fan, and P. Erhart, Calorine: A Python package for constructing and sampling neuroevolution potential models, Journal of Open Source Software **9**, 6264 (2024).

[33] A. Y. Toukmaji and J. A. Board, Ewald summation techniques in perspective: a survey, Computer Physics Communications **95**, 73 (1996).

[34] Z. Fan, L. F. C. Pereira, H.-Q. Wang, J.-C. Zheng, D. Donadio, and A. Harju, Force and heat current formulas for many-body potentials in molecular dynamics simulations with applications to thermal conductivity calculations, Physical Review B **92**, 094301 (2015).

[35] D. M. Heyes, Pressure tensor of partial-charge and point-dipole lattices with bulk and surface geometries, Physical Review B **49**, 755 (1994).

[36] B. J. Kirby and P. Jungwirth, Charge scaling manifesto: A way of reconciling the inherently macroscopic and microscopic natures of molecular simulations, The Journal of Physical Chemistry Letters **10**, 7531 (2019).

[37] M. P. Allen and D. J. Tildesley, *Computer Simulation of Liquids* (Oxford University Press, 2017).

[38] T. Darden, D. York, and L. Pedersen, Particle mesh Ewald: An $N\log(N)$ method for Ewald sums in large systems, The Journal of Chemical Physics **98**, 10089 (1993).

[39] U. Essmann, L. Perera, M. L. Berkowitz, T. Darden, H. Lee, and L. G. Pedersen, A smooth particle mesh Ewald method, The Journal of Chemical Physics **103**, 8577 (1995).

[40] M. Deserno and C. Holm, How to mesh up Ewald sums. I. A theoretical and numerical comparison of various particle mesh routines, The Journal of Chemical Physics **109**, 7678 (1998).

[41] V. Ballenegger, J. J. Cerdà, and C. Holm, How to convert SPME to P3M: Influence functions and error estimates, Journal of Chemical Theory and Computation **8**, 936 (2012).

[42] K. Xu, Y. Hao, T. Liang, P. Ying, J. Xu, J. Wu, and Z. Fan, Accurate prediction of heat conductivity of water by a neuroevolution potential, The Journal of Chemical Physics **158**, 204114 (2023).

[43] N. Xu, P. Rosander, C. Schäfer, E. Lindgren, N. Österbacka, M. Fang, W. Chen, Y. He, Z. Fan, and P. Erhart, Tensorial properties via the neuroevolution potential framework: Fast simulation of infrared and raman spectra, Journal of Chemical Theory and Computation **20**, 3273 (2024).

[44] L. Zhang, H. Wang, R. Car, and W. E, Phase diagram of a deep potential water model, Physical Review Letters **126**, 236001 (2021).

[45] J. Sun, A. Ruzsinszky, and J. P. Perdew, Strongly constrained and appropriately normed semilocal density functional, Physical Review Letters **115**, 036402 (2015).

[46] G. Kresse and J. Furthmüller, Efficiency of ab-initio total energy calculations for metals and semiconductors using a plane-wave basis set, Computational Materials Science **6**, 15 (1996).

[47] P. E. Blöchl, Projector augmented-wave method, Physical Review B **50**, 17953 (1994).

[48] G. Kresse and D. Joubert, From ultrasoft pseudopotentials to the projector augmented-wave method, Physical Review B **59**, 1758 (1999).

[49] I. Thormählen, J. Straub, and U. Grigull, Refractive index of water and its dependence on wavelength, temperature, and density, Journal of Physical and Chemical Reference Data **14**, 933 (1985).

[50] A. H. Harvey, J. S. Gallagher, and J. M. H. L. Sengers, Revised formulation for the refractive index of water and steam as a function of wavelength, temperature and density, Journal of Physical and Chemical Reference Data **27**, 761 (1998).

[51] E. W. Lemmon, I. H. Bell, M. L. Huber, and M. O. McLinden, Thermophysical properties of fluid systems, in *NIST Chemistry WebBook, NIST Standard Reference Database Number 69*, edited by P. J. Linstrom and W. G. Mallard (National Institute of Standards and Technology, Gaithersburg MD, 20899, retrieved January 11, 2026).

[52] P. Ying, W. Zhou, L. Svensson, E. Berger, E. Fransson, F. Eriksson, K. Xu, T. Liang, J. Xu, B. Song, S. Chen, P. Erhart, and Z. Fan, Highly efficient path-integral molecular dynamics simulations with gpumd using neuroevolution potentials: Case studies on thermal properties of materials, Journal of Chemical Physics **162**, 064109 (2025).

[53] H. D. Downing and D. Williams, Optical constants of water in the infrared, Journal of Geophysical Research **80**, 1656 (1975).

[54] J.-J. Max and C. Chapados, Isotope effects in liquid water by infrared spectroscopy. III. H_2O and D_2O spectra from 6000 to 0 cm^{-1}, Journal of Chemical Physics **131**, 184505 (2009).

[55] Y. Chen, E. Rangasamy, C. R. dela Cruz, C. Liang, and K. An, A study of suppressed formation of low-conductivity phases in doped $Li_7La_3Zr_2O_{12}$ garnets by in situ neutron diffraction, Journal of Materials Chemistry A **3**, 22868 (2015).

[56] F. Han, Y. Zhu, X. He, Y. Mo, and C. Wang, Electrochemical stability of $Li_{10}GeP_2S_{12}$ and $Li_7La_3Zr_2O_{12}$ solid electrolytes, Advanced Energy Materials **6**, 1501590 (2016).

[57] Z. Yan and Y. Zhu, Impact of lithium nonstoichiometry on ionic diffusion in tetragonal garnet-type $Li_7La_3Zr_2O_{12}$, Chemistry of Materials **36**, 11551 (2024).

[58] J. P. Perdew, A. Ruzsinszky, G. I. Csonka, O. A. Vydrov, G. E. Scuseria, L. A. Constantin, X. Zhou, and K. Burke, Restoring the density-gradient expansion for exchange in solids and surfaces, Physical Review Letters **100**, 136406 (2008).

[59] G. J. Martyna, M. E. Tuckerman, D. J. Tobias, and M. L. Klein, Explicit reversible integrators for extended sys-

tems dynamics, Molecular Physics **87**, 1117 (1996).
[60] W. J. Merz, The electric and optical behavior of $BaTiO_3$ single-domain crystals, Physical Review **76**, 1221 (1949).
[61] T. S. Benedict and J. L. Durand, Dielectric properties of single domain crystals of $BaTiO_3$ at microwave frequencies, Physical Review **109**, 1091 (1958).
[62] H. H. Wieder, Electrical behavior of barium titanate single crystals at low temperatures, Physical Review **99**, 1161 (1955).
[63] Y. Wang and W. Lai, Phase transition in lithium garnet oxide ionic conductors $Li_7La_3Zr_2O_{12}$: The role of Ta substitution and H_2O/CO_2 exposure, Journal of Power Sources **275**, 612 (2015).
[64] E. Fransson, M. Slabanja, P. Erhart, and G. Wahnström, dynasor–a tool for extracting dynamical structure factors and current correlation functions from molecular dynamics simulations, Advanced Theory and Simulations **4**, 2000240 (2021).
[65] E. Berger, E. Fransson, F. Eriksson, E. Lindgren, G. Wahnström, T. H. Rod, and P. Erhart, Dynasor 2: From simulation to experiment through correlation functions, Computer Physics Communications **316**, 109759 (2025).
[66] L. Gigli, M. Veit, M. Kotiuga, G. Pizzi, N. Marzari, and M. Ceriotti, Thermodynamics and dielectric response of $BaTiO_3$ by data-driven modeling, npj Computational Materials **8**, 209 (2022).
[67] E. Lindgren, A. J. Jackson, E. Fransson, E. Berger, S. Rudić, G. Škoro, R. Turanyi, S. Mukhopadhyay, and P. Erhart, Predicting neutron experiments from first principles: A workflow powered by machine learning, Journal of Materials Chemistry A **13**, 25509 (2025).
[68] J. W. Furness, A. D. Kaplan, J. Ning, J. P. Perdew, and J. Sun, Accurate and numerically efficient r2SCAN meta-generalized gradient approximation, The Journal of Physical Chemistry Letters **11**, 8208 (2020).
[69] T. Hashimoto and H. Moriwake, Dielectric properties of $BaTiO_3$ by molecular dynamics simulations using a shell model, Molecular Simulation **41**, 1074 (2015).
[70] Y. Jiang, E. Parsonnet, A. Qualls, W. Zhao, S. Susarla, D. Pesquera, A. Dasgupta, M. Acharya, H. Zhang, T. Gosavi, C.-C. Lin, D. E. Nikonov, H. Li, I. A. Young, R. Ramesh, and L. W. Martin, Enabling ultra-low-voltage switching in $BaTiO_3$, Nature Materials **21**, 779 (2022).
[71] Y.-H. Shin, I. Grinberg, I.-W. Chen, and A. M. Rappe, Nucleation and growth mechanism of ferroelectric domain-wall motion, Nature **449**, 881 (2007).
[72] A. Togo, L. Chaput, T. Tadano, and I. Tanaka, Implementation strategies in phonopy and phono3py, Journal of Physics: Condensed Matter **35**, 353001 (2023).
[73] A. Togo, First-principles phonon calculations with phonopy and phono3py, Journal of the Physical Society of Japan **92**, 012001 (2023).
[74] J. A. Thomas, J. E. Turney, R. M. Iutzi, C. H. Amon, and A. J. H. McGaughey, Predicting phonon dispersion relations and lifetimes from the spectral energy density, Physical Review B **81**, 081411 (2010).
[75] A. Z. Benbouzid, M. P. Gomes, I. Costa, O. Gharbi, N. Pébère, J. L. Rossi, M. T. T. Tran, B. Tribollet, M. Turmine, and V. Vivier, A new look on the corrosion mechanism of magnesium: An EIS investigation at different pH, Corrosion Science **205**, 110463 (2022).
[76] Z. Liu, J. Sha, G.-L. Song, Z. Wang, and Y. Zhang, Understanding magnesium dissolution through machine learning molecular dynamics, Chemical Engineering Journal **516**, 163578 (2025).
[77] Z. Liu, J. Bao, J. Sha, and Z. Zhang, Modulation of the discharge and corrosion properties of aqueous Mg–air batteries by alloying from first-principles theory, The Journal of Physical Chemistry C **127**, 10062 (2023).
[78] H. Yu, L. Hong, S. Chen, X. Gong, and H. Xiang, Capturing long-range interaction with reciprocal space neural network (2022), arXiv:2211.16684 [cond-mat.mtrl-sci].
[79] P. Loche, K. K. Huguenin-Dumittan, M. Honarmand, Q. Xu, E. Rumiantsev, W. B. How, M. F. Langer, and M. Ceriotti, Fast and flexible long-range models for atomistic machine learning, The Journal of Chemical Physics **162**, 142501 (2025).
[80] Y. Ji, J. Liang, and Z. Xu, Machine-learning interatomic potentials for long-range systems, Physical Review Letters **135**, 178001 (2025).

Supporting Information

qNEP: A highly efficient neuroevolution potential with dynamic charges for large-scale atomistic simulations

Zheyong Fan,[1,2,*] Benrui Tang,[1] Esmée Berger,[3] Ethan Berger,[3] Erik Fransson,[3] Ke Xu,[1] Zihan Yan,[4] Zhoulin Liu,[5] Zichen Song,[6,7] Haikuan Dong,[1] Shunda Chen,[8] Lei Li,[6] Ziliang Wang,[9] Yizhou Zhu,[4] Julia Wiktor,[3] and Paul Erhart[3,10,†]

[1] College of Physical Science and Technology, Bohai University, Jinzhou, P. R. China
[2] Suzhou Laboratory, Suzhou, Jiangsu 215123, P. R. China
[3] Chalmers University of Technology, Department of Physics, 41296 Gothenburg, Sweden
[4] Department of Materials Science and Engineering, Westlake University, Hangzhou, Zhejiang 310030, China
[5] School of Science, Harbin Institute of Technology, Shenzhen 518055, Guangdong, P. R. China
[6] Shenzhen Key Laboratory of Micro/Nano-Porous Functional Materials (SKLPM), Department of Materials Science and Engineering, Southern University of Science and Technology, Shenzhen 518055, China
[7] Department of Materials Science and Engineering, City University of Hong Kong, Hong Kong SAR, China
[8] Department of Civil and Environmental Engineering, George Washington University, Washington, DC 20052, USA
[9] National Engineering Laboratory for Reducing Emissions from Coal Combustion, Shandong Key Laboratory of Green Thermal Power and Carbon Reduction, Shandong University, Jinan, Shandong, P. R. China
[10] Wallenberg Initiative Materials Science for Sustainability, Chalmers University of Technology, 41926 Gothenburg, Sweden
* brucenju@gmail.com
† erhart@chalmers.se

Contents

Supplementary Notes

Supplementary Note 1: General tools

The GPUMD package was used for training neuroevolution potential (NEP) and qNEP models as well as for running all molecular dynamics (MD) simulations (1). The CALORINE package was used to prepare model training and analyze models, as well as to analyze the results of the MD simulations (2). The NEP and qNEP models constructed in this work as well as the reference data used for their training and validation have been deposited on Zenodo under accession code 10.5281/zenodo.18335947.

Supplementary Note 2: Training of water models

We trained NEP and qNEP models in both mode 1 and 2 using the separable natural evolution strategy (SNES) algorithm (3). The radial and angular cutoffs were set to 6 Å and 4 Å, respectively, the descriptor was expressed using $n_{\max} = (4, 4)$ and $l_{\max} = (4, 2)$, and the dimension of the hidden layer was set to 30. We employed a two stage process, in which we first trained the models for 150×10^3 SNES generations emphasizing the contribution of the forces to the loss term ($\lambda_f = 10$, $\lambda_e = 1$, $\lambda_v = 0.1$) followed by another 150×10^3 generations during which the weight of the forces was reduced and the weight of the energies was increased ($\lambda_f = 5$, $\lambda_e = 5$, $\lambda_v = 0.1$). This procedure led to higher accuracies for both energies and forces compared to a single stage optimization of the same total length. For the qNEP models we additionally set the weight of the charge neutrality condition ($\lambda_q = 0.5$) and the Born effective charges (BECs) ($\lambda_{\mathcal{Z}} = 3$), using the same values for both stages. For $\lambda_{\mathcal{Z}}$ we tested values of 1, 3, and 5. Increasing this value reduces the error of the BEC prediction (Figure S2) but if the value becomes too large it negatively affects the other predictions, specifically the forces. The final value of $\lambda_{\mathcal{Z}}$ balances the accuracy of the forces and the BECs.

Supplementary Note 3: DFT calculations for water

The energies, forces, and virials for the reference structures were taken from earlier work (4, 5). For 194 of these structures, we calculated BECs. For consistency with the existing reference data, we employed the strongly constrained and appropriately normed semilocal density functional (SCAN) functional (6) as implemented in the Vienna ab-initio simulation package (7) using projector-augmented wave (8, 9) setups. We tested plane wave energy cutoffs up to 1000 eV and found that 800 eV is sufficient to converge the components of the BEC tensor to below 10^{-3} e (Figure S3). The Brillouin zone was sampled with Γ-centered automatically generated **k**-point grids with a maximum spacing of 0.5/Å.

Supplementary Note 4: Simulations of water

All production runs were carried out using a system comprising 13 000 H_2O molecules at the experimental density at 0.1 MPa (=1 bar) and the respective temperature (10). For reference, at 300 K the density is 996.56 kg/m^3 and it drops to 967.40 kg/m^3.

All systems were equilibrated for 200 ps in the NVT ensemble using a time step of 0.5 fs.

The radial partial radial distribution functions in the classical limit were extracted from the MD trajectory of the equilibrated systems. To incorporate quantum effects path-integral molecular dynamics (PIMD) simulations were carried out (11). In these simulations we used a time step of 0.5 fs and 64 beads. The simulations were run for 200 ps and the partial radial distribution function were sampled every 5 ps.

For the calculation of the infrared spectra, the dynamics were sampled for 400 ps using a time step of 0.1 fs. During the latter part the polarization was evaluated every 0.5 fs using both the BECs and the TNEP model for the polarization from Ref. 12. The autocorrelation functions (ACFs) of the ionic electric current from the BECs and the polarization from the TNEP model were evaluated and analyzed using the DYNASOR package to obtain the infrared spectra. To improve statistics we ran five simulations for each temperature.

Supplementary Note 5: Training of LLZO models

We trained NEP and qNEP models in both mode 1 and mode 2 using the SNES algorithm (3). To this end, we used the data set of Yan and Zhu (13), which comprises 1978 configurations of pristine LLZO with energies, forces, and stresses computed using the PBEsol exchange–correlation functional (14).

The radial and angular cutoffs were set to 5 Å each, the descriptor was expressed using $n_{\max} = (4, 4)$ and $l_{\max} = (4, 2, 1)$, and the dimension of the hidden layer was set to 30. The universal Ziegler-Biersack-Littmark (ZBL) potential with an outer cutoff of 2 Å and an inner cutoff of 1 Å was applied to improve the robustness of the machine-learned interatomic potential (MLIP). Models were trained for 100×10^3 SNES generations using $\lambda_f = 1$, $\lambda_e = 1$, $\lambda_v = 0.1$, and $\lambda_q = 0.1$.

Supplementary Note 6: Simulations of LLZO

The heating and cooling simulations were carried out in the NPT ensemble using a $6 \times 6 \times 6$ supercell (41 472 atoms) and a time step of 2 fs. The temperature was varied between 200 K and 1200 K over a period of 20 ns. The heat capacity was obtained by taking the numerical derivative of the potential energy after application of a gliding average.

The MD simulations for the ion diffusion utilized a $4\times4\times4$ supercell (12 288 atoms) and Martyna-Tuckerman-Tobias-Klein integrators (15) for sampling the NPT ensemble. The tetragonal and cubic phases were simulated for 2 ns and 1 ns, respectively, using a timestep of 1 fs. The Li diffusivity was calculated from the mean square displacement over time,

$$D = \frac{1}{2Nd\Delta t} \sum_{i=1}^{N} \left\langle |\mathbf{r}_i(t + \Delta t) - \mathbf{r}_i(t)|^2 \right\rangle_t , \tag{1}$$

where N is the total number of diffusing ions, $d = 3$ denotes the dimension of the system, $r_i(t)$ is the displacement of ion i at time t, and the bracket represents averaging over t. The ionic conductivity (σ) is then determined using the Nernst-Einstein relation

$$\sigma = \frac{nq^2}{k_{\mathrm{B}}T} D, \tag{2}$$

where n is the number of mobile ions per unit volume, q is the ionic charge, k_B is the Boltzmann constant, and T is the temperature.

Supplementary Note 7: Training of barium titanate models

An initial set of 639 structures was taken from Ref. 16 (see `https://doi.org/10.5281/zenodo.15283532` for the Zenodo record). This set comprises fully relaxed bulk structures covering various phases including rhombohedral, orthorhombic, tetragonal, cubic, and hexagonal variants across a wide range of volumes. It also features rattled structures, structures with controlled displacements along the ferroelectric modes, as well as structures from two generations of active learning. This set was augmented by adding structures with BECs. These were obtained by running MD simulations using the NEP model previously trained in Ref. 16. In total, 1193 structures of $\sqrt{2} \times \sqrt{2} \times 2$ supercells (20 atoms) were obtained at temperatures between 50 K and 600 K to sample all four phases. The final reference set comprised 1832 structures, corresponding to a total of 36 540 atoms.

The radial and angular cutoffs were set to 6 Å and 4 Å, respectively, the descriptor was expressed using $n_{\max} = (8, 6)$ and $l_{\max} = (4, 0)$, and the dimension of the hidden layer was set to 40. We trained NEP and qNEP models in both mode 1 and mode 2 using the SNES algorithm (3). Models were trained for 500×10^3 SNES generations using $\lambda_f = 1$, $\lambda_e = 1$, $\lambda_v = 0.1$, $\lambda_q = 0.1$, and $\lambda_{\mathcal{Z}} = 0.1$.

Supplementary Note 8: DFT calculations for barium titanate

The energies, forces, and virials for the initial 639 reference structures were taken from earlier work (16). For consistency, energies, forces and virials for the additional 1193 structures are obtained using the r2SCAN exchange-correlation functional (17) as implemented in the Vienna ab-initio simulation package (7). The BECs were then obtained using density functional perturbation theory and the PBEsol functional (14).

Supplementary Note 9: Simulations of barium titanate

First, cooling simulations were performed in the NPT ensemble using the qNEP model and starting from a perfectly cubic $20 \times 20 \times 20$ supercell (40 000 atoms). A time step of 1 fs was used for all simulations. After 100 ps of equilibration at 500 K, the temperature was linearly decreased to 50 K over 45 ns, resulting in a cooling rate of 10 K/ns. The final structure was then used as the starting point for a heating run with the same heating rate of 10 K/ns.

For both cooling and heating simulations, 100 structures were saved along the trajectory and subsequently used to obtain the lattice parameters, the spontaneous polarization and the dielectric function as a function of temperature. The spontaneous polarization $\mathbf{P}$ was obtained as

$$P_\alpha = \frac{1}{V}\sum_{i=1}^{N}\sum_{\beta}\mathcal{Z}_{i\alpha\beta}u_{i\beta}, \tag{3}$$

where V is the volume and $\mathbf{u}_i = \mathbf{r}_i - \mathbf{r}_0$ denotes the displacement of atom i from its reference position $\mathbf{r}_0$ in the cubic structure. The dielectric constants were obtained as

$$\varepsilon_{\alpha\beta} = 4\pi\frac{P_\alpha(E\cdot\hat{e}_\beta) - P_\alpha(0)}{E}, \tag{4}$$

where $P_\alpha(\mathbf{E})$ denotes the polarization in the Cartesian direction α when applying an external electric field $\mathbf{E}$. In practice, we ran MD simulations both without and with electric field in each Cartesian direction, and computed the average polarization as $P_\alpha(\mathbf{E})$. The strength of the electric field was set to 1 mV/Å.

Polarization–electric field (P–E) hysteresis loops were obtained by running MD simulations at constant temperature but with the field varying from 0.2 V/nm to −0.2 V/nm over 2 ns (backward) and again from −0.2 V/nm to 0.2 V/nm over 2 ns (forward), corresponding to a frequency of 500 MHz. The atomic positions were sampled every 20 ps and used to obtain the polarization via Eq. (3).

The imaginary part of the dielectric function was obtained from the Fourier transform of the time ACF $\langle\dot{\mathbf{P}}(0)\cdot\dot{\mathbf{P}}(t)\rangle$. The time derivative of the polarization $\dot{\mathbf{P}}(t)$ was sampled every 20 fs along a 2 ns MD trajectory at constant temperature and volume, and calculated using Eq. (32) of the main text. The real part of the dielectric function was subsequently obtained via a Kramer-Kronig transformation.

Supplementary Note 10: Phonons in barium titanate

The harmonic phonons were evaluated using PHONOPY in supercells (320 atoms) of $4\times4\times4$ repetitions of the cubic primitive cell (18, 19). The phonon spectral energy density (20) was evaluated from MD simulations in the NVE ensemble at 500 K in the cubic phase using supercells of $36\times36\times36$ repetitions (233 280 atoms). The simulations were run using a time step of 1 fs, using lattice parameters from the NPT runs. The system was first equilibrated for 100 ps in the NVT ensemble, followed by 150 ps in the NVE ensemble where velocities were saved to file every 15 fs. The spectral energy density was then computed from the velocities using DYNASOR (21, 22).

Supplementary Note 11: Training of Mg–O–H models

The reference dataset contained 2809 structures, obtained from Ref. 23, for which the energies, forces, and stresses were calculated using density-functional theory (DFT) and the PBE exchange–correlation functional (24). This dataset includes metallic magnesium, aqueous solutions, hydrogen gas, magnesium oxides, magnesium hydrides, magnesium hydroxides, and interfacial structures between magnesium metal and water. This dataset was augmented with D3 dispersion corrections for training.

The radial and angular cutoffs were set to 6.5 Å and 4.5 Å, respectively, the descriptor was expressed using $n_{\max} = (4, 4)$ and $l_{\max} = (4, 2)$, and the dimension of the hidden layer was set to 30. We trained a NEP model and a qNEP model in mode 2 using the SNES algorithm (3). Models were trained for 100×10^3 SNES generations using $\lambda_f = 1$, $\lambda_e = 1$, $\lambda_v = 0.1$, and $\lambda_q = 0.1$.

Supplementary Note 12: Simulations of Mg-water interface

A comprehensive analysis of the corrosion of Mg in water was recently presented in Ref. 23 based on a (charge unaware) NEP model. Since the detailed trajectories are determined by a series of rare events, a comprehensive understanding of this system requires a large number of simulations and analysis. Here, we are focused on the development of the qNEP approach. Rather than repeating the comprehensive analysis from Ref. 23 we therefore applied our qNEP model to analyze a specific trajectory from this earlier work.

The MD simulation shown in the main text was taken from Ref. 23 and generated using the NEP model developed in the same work. While the potential was fitted without DFT-D3 (PBE) dispersion corrections, the latter were applied during the MD run to improve the description of the interactions with the water environment. The qNEP model (Note 11) was used to analyze the evolution of the charge distribution.

The simulation shown contains approximately 2430 atoms and a highly reactive stepped surface of magnesium, the construction of which is described in Ref. 25. To ensure a sufficiently reactive environment, the H_2O:Mg ratio was chosen to be greater than two. The system was first relaxed in the NPT ensemble at 300 K

and 1 bar, followed by a production run in the NVT ensemble at 700 K. The system was simulated for 5 ns using a time step of 0.5 fs.

Supplementary Figures

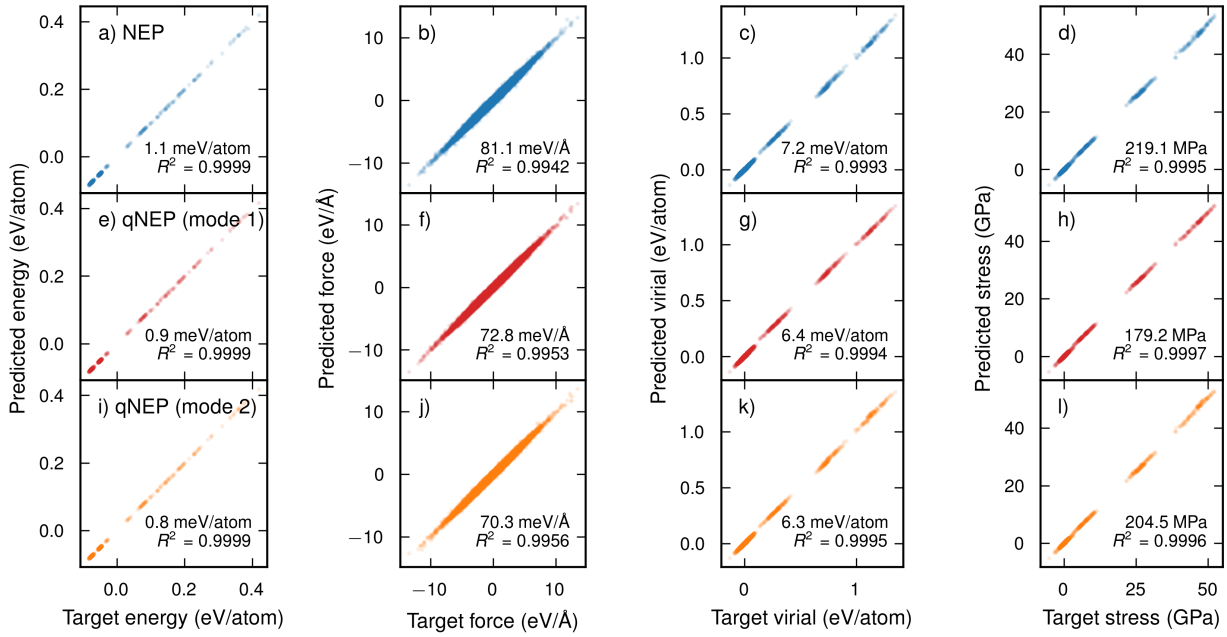

Figure S1: Energy, forces, virials, and stresses of water configurations (validation set) for NEP and qNEP models compared to target data from DFT calculations.

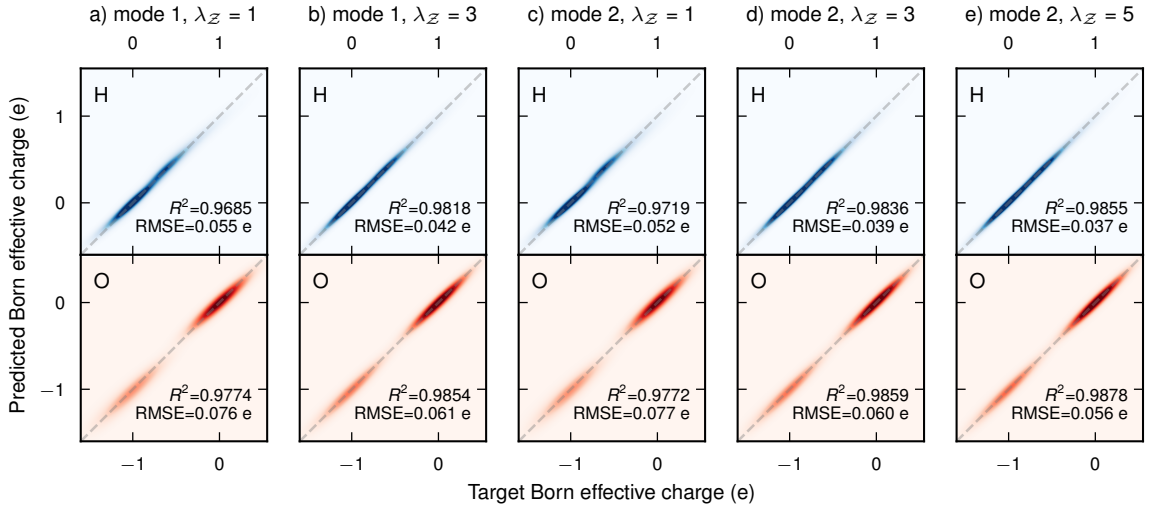

Figure S2: Kernel density estimate plots of BECs in water predicted by qNEP models trained using mode 1 and mode 2 as well as different choices for the $\lambda_{\mathcal{Z}}$ parameter compared to target data from DFT calculations. The latter controls the weight of the BECs in the loss function. The insets provide the respective coefficients of correlation (R^2) and root-mean-square errors (RMSEs).

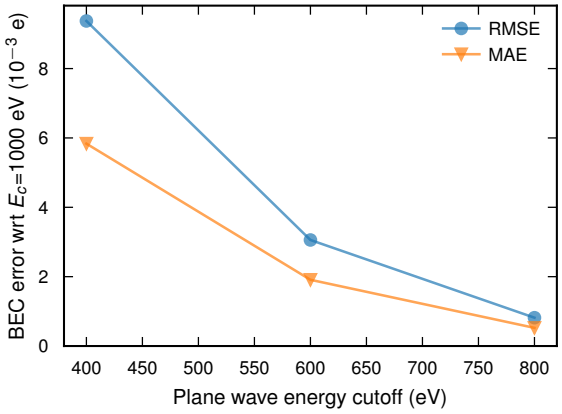

Figure S3: Convergence of components of the BEC tensor in water with plane-wave energy cutoff.

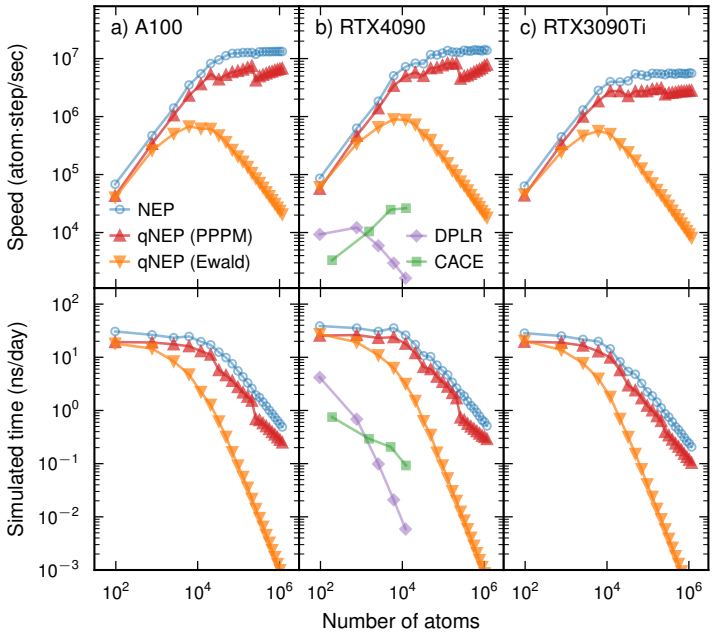

Figure S4: Computational speed (top) and corresponding simulated time (bottom) for NEP and qNEP models for water on different GPUs. Simulations were carried out at 300 K and a density of 1000 kg/m^3 using a time step of 0.5 fs.

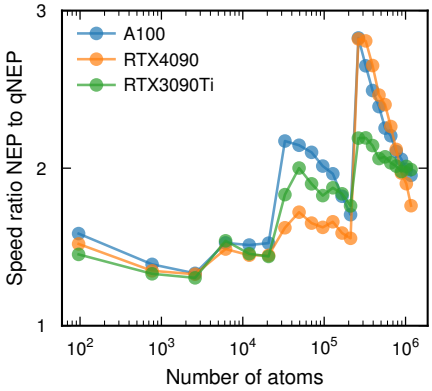

Figure S5: Ratio of the computational speed of NEP and qNEP models (mode 2) for water on different GPUs. Simulations were carried out at 300 K and a density of 1000 kg/m^3.

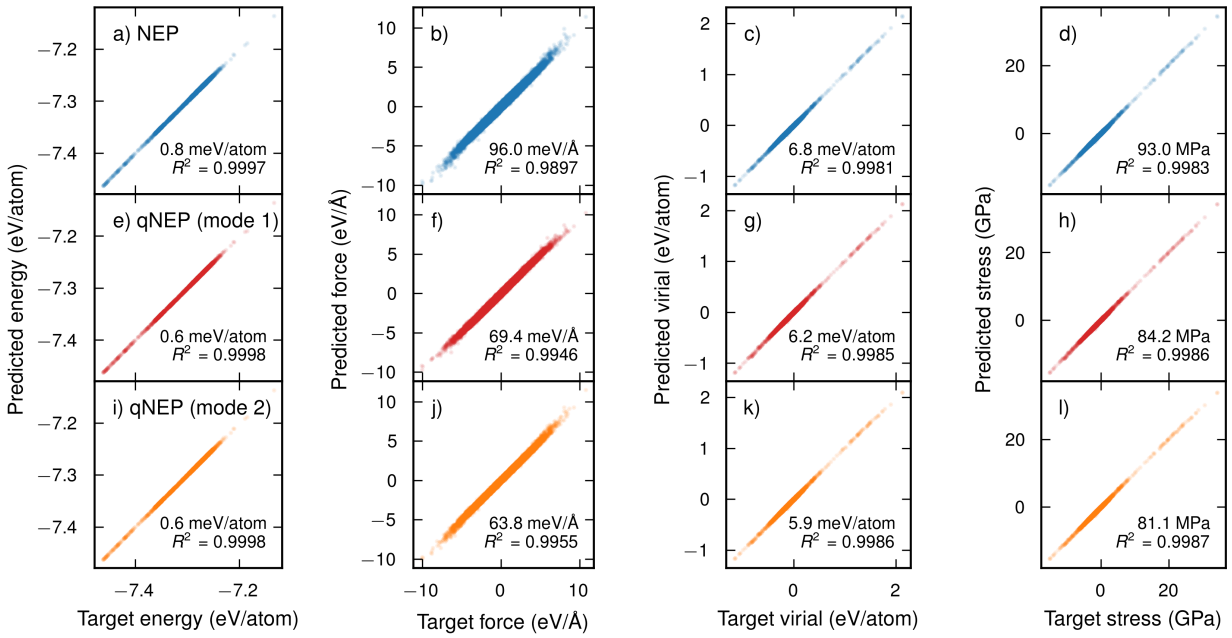

Figure S6: Parity plots for energy, forces, virials, and stresses for the reference configurations for LLZO for NEP and qNEP models compared to target data from DFT calculations.

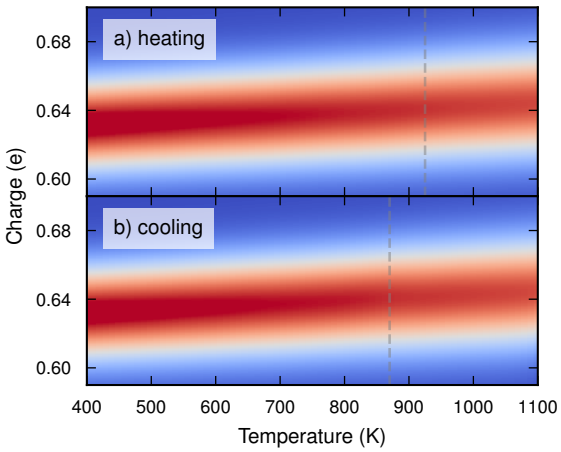

Figure S7: Charge distribution of Li as a function of temperature LLZO from kernel density estimates from (a) heating and (b) cooling runs.

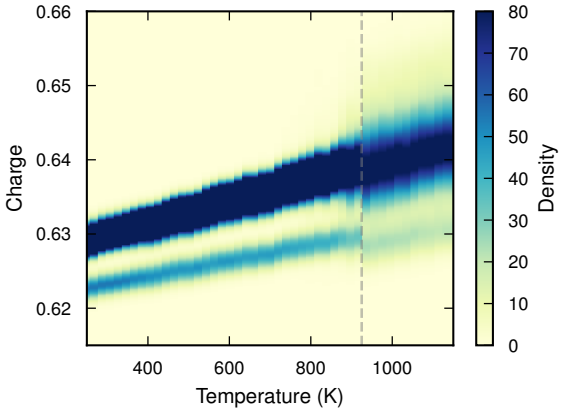

Figure S8: Charge distribution of Li in LLZO as a function of temperature from kernel density estimates. The snapshots were obtained at different temperatures along a heating run and subsequently relaxed with the cell metric fixed. Note the abrupt change in the charge distribution at the transition from the low-temperature *t*-LLZO to the high-temperature *c*-LLZO phase.

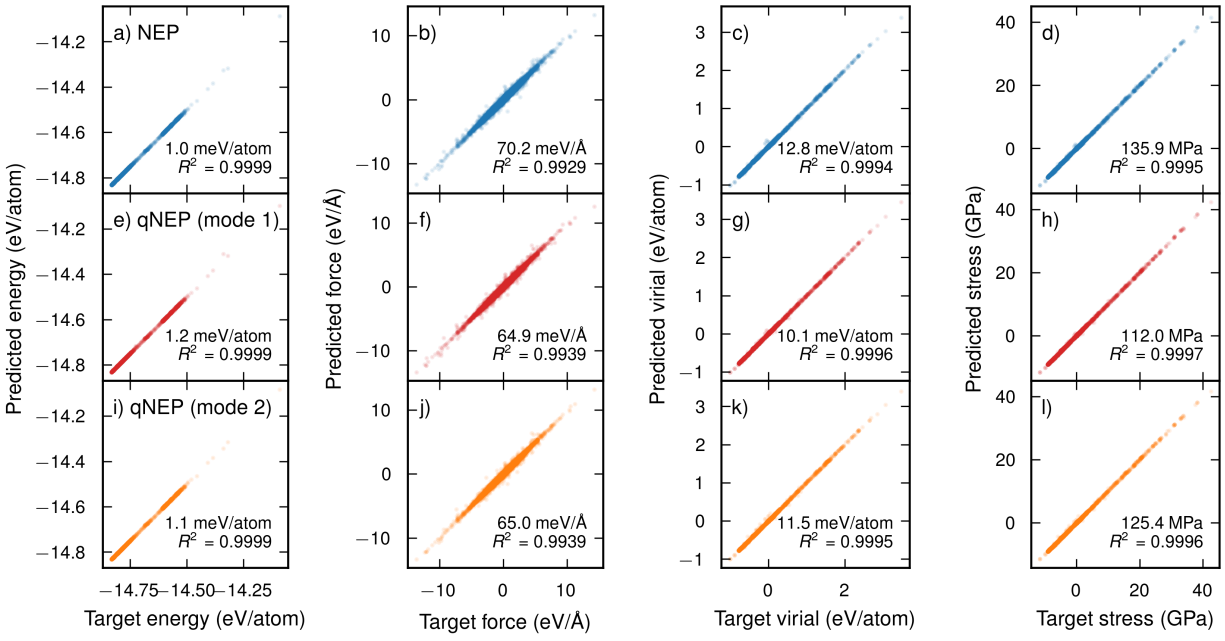

Figure S9: Parity plots for energy, forces, virials, and stresses for the reference configurations for $BaTiO_3$ for NEP and qNEP models compared to target data from DFT calculations.

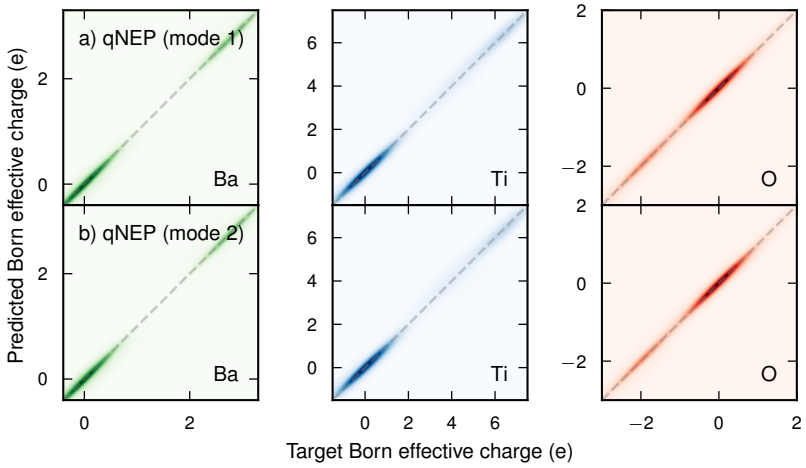

Figure S10: Kernel density estimate plots of BECs in $BaTiO_3$ predicted by qNEP models trained using (a) mode 1 and (b) mode 2 in comparison with target data from DFT calculations.

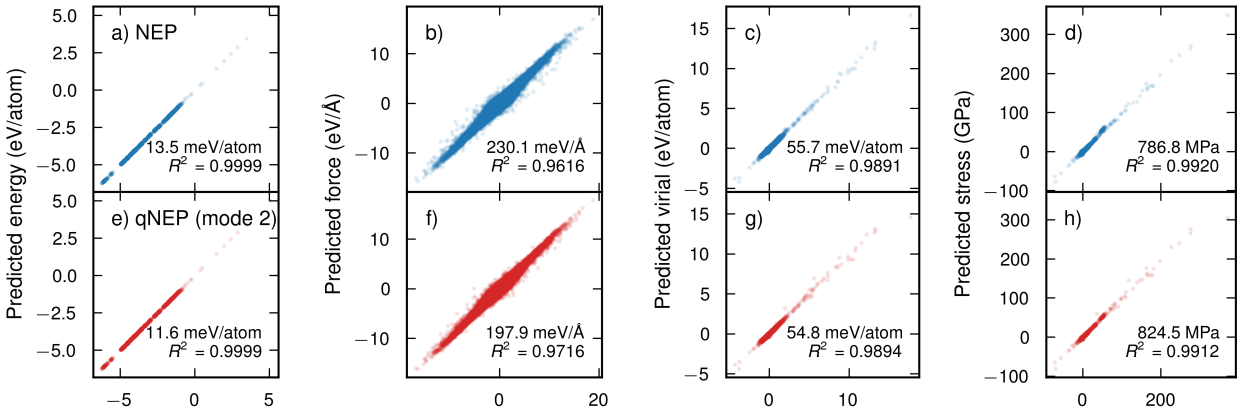

Figure S11: Parity plots for energy, forces, virials, and stresses for the reference configurations for the Mg–O–H system from NEP and qNEP models, where the latter has been trained using mode 2, compared to target data obtained from DFT calculations.

Supplementary References

[1] K. Xu, H. Bu, S. Pan, E. Lindgren, Y. Wu, Y. Wang, J. Liu, K. Song, B. Xu, Y. Li, T. Hainer, L. Svensson, J. Wiktor, R. Zhao, H. Huang, C. Qian, S. Zhang, Z. Zeng, B. Zhang, B. Tang, Y. Xiao, Z. Yan, J. Shi, Z. Liang, J. Wang, T. Liang, S. Cao, Y. Wang, P. Ying, N. Xu, C. Chen, Y. Zhang, Z. Chen, X. Wu, W. Jiang, E. Berger, Y. Li, S. Chen, A. J. Gabourie, H. Dong, S. Xiong, N. Wei, Y. Chen, J. Xu, F. Ding, Z. Sun, T. Ala-Nissila, A. Harju, J. Zheng, P. Guan, P. Erhart, J. Sun, W. Ouyang, Y. Su, and Z. Fan, *GPUMD 4.0: A high-performance molecular dynamics package for versatile materials simulations with machine-learned potentials,* Materials Genome Engineering Advances **3**, e70028 (2025). doi:doi:10.1002/mgea.70028.

[2] E. Lindgren, M. Rahm, E. Fransson, F. Eriksson, N. Österbacka, Z. Fan, and P. Erhart, *Calorine: A Python package for constructing and sampling neuroevolution potential models,* Journal of Open Source Software **9**, 6264 (2024). doi:10.21105/joss.06264.

[3] T. Schaul, T. Glasmachers, and J. Schmidhuber, *High dimensions and heavy tails for natural evolution strategies,* in *Proceedings of the 13th Annual Conference on Genetic and Evolutionary Computation*, GECCO '11, (New York, NY, USA), 845852, Association for Computing Machinery, 2011. doi:10.1145/2001576.2001692.

[4] L. Zhang, H. Wang, R. Car, and W. E, *Phase diagram of a deep potential water model,* Physical Review Letters **126**, 236001 (2021). doi:10.1103/PhysRevLett.126.236001.

[5] K. Xu, Y. Hao, T. Liang, P. Ying, J. Xu, J. Wu, and Z. Fan, *Accurate prediction of heat conductivity of water by a neuroevolution potential,* The Journal of Chemical Physics **158**, 204114 (2023). doi:10.1063/5.0147039.

[6] J. Sun, A. Ruzsinszky, and J. P. Perdew, *Strongly constrained and appropriately normed semilocal density functional,* Physical Review Letters **115**, 036402 (2015). doi:10.1103/PhysRevLett.115.036402.

[7] G. Kresse and J. Furthmüller, *Efficiency of ab-initio total energy calculations for metals and semiconductors using a plane-wave basis set,* Computational Materials Science **6**, 15 (1996). doi:10.1016/0927-0256(96)00008-0.

[8] P. E. Blöchl, *Projector augmented-wave method,* Physical Review B **50**, 17953 (1994). doi:10.1103/PhysRevB.50.17953.

[9] G. Kresse and D. Joubert, *From ultrasoft pseudopotentials to the projector augmented-wave method,* Physical Review B **59**, 1758 (1999). doi:10.1103/PhysRevB.59.1758.

[10] E. W. Lemmon, I. H. Bell, M. L. Huber, and M. O. McLinden, *Thermophysical Properties of Fluid Systems,* in *NIST Chemistry WebBook, NIST Standard Reference Database Number 69*, edited by P. J. Linstrom and W. G. Mallard (Gaithersburg MD, 20899: National Institute of Standards and Technology, retrieved January 11, 2026). doi:10.18434/T4D303.

[11] P. Ying, W. Zhou, L. Svensson, E. Berger, E. Fransson, F. Eriksson, K. Xu, T. Liang, J. Xu, B. Song, S. Chen, P. Erhart, and Z. Fan, *Highly efficient path-integral molecular dynamics simulations with GPUMD using neuroevolution potentials: Case studies on thermal properties of materials,* Journal of Chemical Physics **162**, 064109 (2025). doi:10.1063/5.0241006.

[12] N. Xu, P. Rosander, C. Schäfer, E. Lindgren, N. Österbacka, M. Fang, W. Chen, Y. He, Z. Fan, and P. Erhart, *Tensorial properties via the neuroevolution potential framework: Fast simulation of infrared and Raman spectra,* Journal of Chemical Theory and Computation **20**, 3273 (2024). doi:10.1021/acs.jctc.3c01343.

[13] Z. Yan and Y. Zhu, *Impact of lithium nonstoichiometry on ionic diffusion in tetragonal garnet-type $Li_7La_3Zr_2O_{12}$,* Chemistry of Materials **36**, 11551 (2024). doi:10.1021/acs.chemmater.4c02454.

[14] J. P. Perdew, A. Ruzsinszky, G. I. Csonka, O. A. Vydrov, G. E. Scuseria, L. A. Constantin, X. Zhou, and K. Burke, *Restoring the density-gradient expansion for exchange in solids and surfaces,* Physical Review Letters **100**, 136406 (2008). doi:10.1103/PhysRevLett.100.136406.

[15] G. J. Martyna, M. E. Tuckerman, D. J. Tobias, and M. L. Klein, *Explicit reversible integrators for extended systems dynamics,* Molecular Physics **87**, 1117 (1996). doi:10.1080/00268979600100761.

[16] E. Lindgren, A. J. Jackson, E. Fransson, E. Berger, S. Rudić, G. Škoro, R. Turanyi, S. Mukhopadhyay, and P. Erhart, *Predicting neutron experiments from first principles: A workflow powered by machine learning,* Journal of Materials Chemistry A **13**, 25509 (2025). doi:10.1039/D5TA03325J.

[17] J. W. Furness, A. D. Kaplan, J. Ning, J. P. Perdew, and J. Sun, *Accurate and numerically efficient r2SCAN meta-generalized gradient approximation,* The Journal of Physical Chemistry Letters **11**, 8208 (2020). doi:10.1021/acs.jpclett.0c02405.

[18] A. Togo, L. Chaput, T. Tadano, and I. Tanaka, *Implementation strategies in phonopy and phono3py,* Journal of Physics: Condensed Matter **35**, 353001 (2023). doi:10.1088/1361-648X/acd831.

[19] A. Togo, *First-principles phonon calculations with Phonopy and Phono3py,* Journal of the Physical Society of Japan **92**, 012001 (2023). doi:10.7566/JPSJ.92.012001.

[20] J. A. Thomas, J. E. Turney, R. M. Iutzi, C. H. Amon, and A. J. H. McGaughey, *Predicting phonon dispersion relations and lifetimes from the spectral energy density,* Physical Review B **81**, 081411 (2010). doi:10.1103/PhysRevB.81.081411.

[21] E. Fransson, M. Slabanja, P. Erhart, and G. Wahnström, *dynasor–A tool for extracting dynamical structure factors and current correlation functions from molecular dynamics simulations,* Advanced Theory and Simulations **4**, 2000240 (2021). doi:10.1002/adts.202000240.

[22] E. Berger, E. Fransson, F. Eriksson, E. Lindgren, G. Wahnström, T. H. Rod, and P. Erhart, *Dynasor 2: From simulation to experiment through correlation functions,* Computer Physics Communications **316**, 109759 (2025). doi:10.1016/j.cpc.2025.109759.

[23] Z. Liu, J. Sha, G.-L. Song, Z. Wang, and Y. Zhang, *Understanding magnesium dissolution through Machine learning molecular dynamics,* Chemical Engineering Journal **516**, 163578 (2025). doi:10.1016/j.cej.2025.163578.

[24] J. P. Perdew, K. Burke, and M. Ernzerhof, *Generalized gradient approximation made simple,* Physical Review Letters **77**, 3865 (1996). doi:10.1103/PhysRevLett.77.3865.

[25] Z. Liu, J. Bao, J. Sha, and Z. Zhang, *Modulation of the discharge and corrosion properties of aqueous Mg–air batteries by alloying from first-principles theory,* The Journal of Physical Chemistry C **127**, 10062 (2023). doi:10.1021/acs.jpcc.3c00111.